Article

Immunity

Innate immune training restores pro-reparative myeloid functions to promote remyelination in the aged central nervous system

Graphical abstract

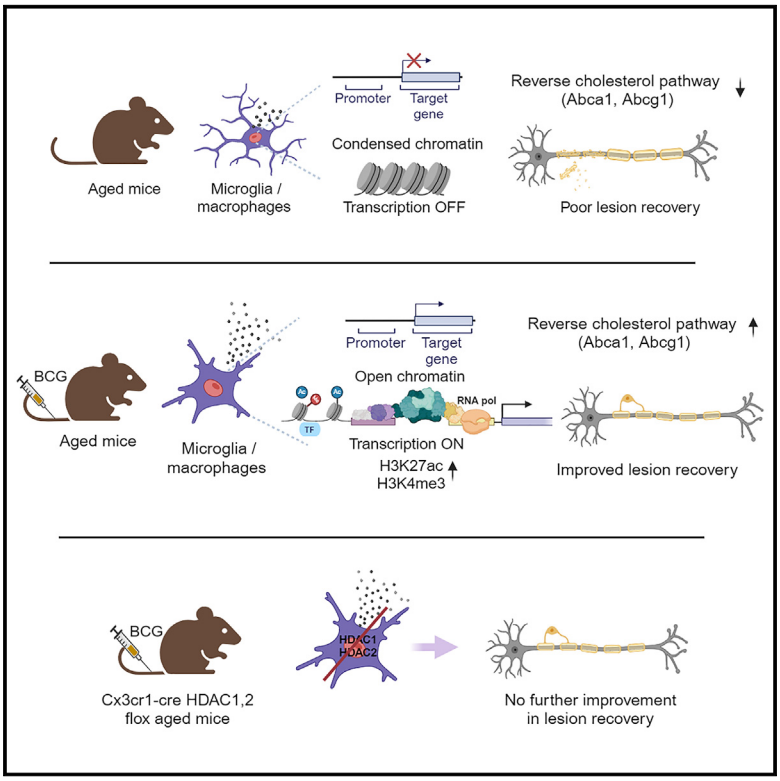

Highlights

- Age-related epigenetic changes impair microglial regenerative function
- Innate immune training enhances myelin debris clearance and lesion recovery
- Conditional deletion of HDAC1/2 in aged microglia enhances lesion recovery
- The innate immune training response is abolished in microglia depleted of HDAC1/2

Authors

Vini Tiwari, Bharat Prajapati, Yaw Asare, ..., Marco Prinz, Ozgun Gokce, Mikael Simons

Correspondence

mikael.simons@dzne.de

In brief

The mechanisms responsible for the age-related decline in remyelination are incompletely understood. Tiwari et al. demonstrate that epigenetic reprogramming via innate immune training with BCG vaccination or conditional deletion of HDAC1/2 in microglia enhances myelin debris clearance and remyelination in aging, offering insights into the mechanisms of age-associated decline in myelin repair.

Tiwari et al., 2024, Immunity 57, 2173–2190
September 10, 2024
https://doi.org/10.1016/j.immuni.2024.07.001

CellPress

Immunity

CellPress
OPEN ACCESS

Article

Innate immune training restores pro-reparative myeloid functions to promote remyelination in the aged central nervous system

Vini Tiwari,[1,2] Bharat Prajapati,[5] Yaw Asare,[4] Alkmini Damkou,[1,2] Hao Ji,[4] Lu Liu,[2,4] Nawraa Naser,[4] Garyfallia Gouna,[1,2] Katarzyna B. Leszczyńska,[6] Jakub Mieczkowski,[6,7] Martin Dichgans,[2,3,4] Qing Wang,[8] Riki Kawaguchi,[8,11] Zechuan Shi,[9] Vivek Swarup,[9] Daniel H. Geschwind,[8] Marco Prinz,[10,12] Ozgun Gokce,[3,4,13,14] and Mikael Simons[1,2,3,4,15,*]

[1]Institute of Neuronal Cell Biology, Technical University Munich, 81377 Munich, Germany
[2]German Center for Neurodegenerative Diseases (DZNE), 81377 Munich, Germany
[3]Munich Cluster of Systems Neurology (SyNergy), 81377 Munich, Germany
[4]Institute for Stroke and Dementia Research, University Hospital of Munich, LMU Munich, 81377 Munich, Germany
[5]Institute of Biomedicine, Sahlgrenska Academy, University of Gothenburg, 41390 Gothenburg, Sweden
[6]Laboratory of Molecular Neurobiology, Nencki Institute of Experimental Biology of the Polish Academy of Sciences, 02093 Warsaw, Poland
[7]3P-Medicine Laboratory, Medical University of Gdańsk, 80211 Gdańsk, Poland
[8]Departments of Neurology and Human Genetics, University of California, Los Angeles, Los Angeles, CA 90095, USA
[9]Department of Neurobiology and Behavior, University of California, Irvine, CA, USA
[10]Institute of Neuropathology, Faculty of Medicine, University of Freiburg, 79085 Freiburg, Germany
[11]Psychiatry, Semel Institute for Neuroscience and Human Behavior, David Geffen School of Medicine, University of California, Los Angeles, Los Angeles, CA 90095, USA
[12]Signalling Research Centres BIOSS and CIBSS, University of Freiburg, 79104 Freiburg, Germany
[13]German Center for Neurodegenerative Diseases (DZNE), 53127 Bonn, Germany
[14]Department of Neurodegenerative Diseases and Geriatric Psychiatry, University Hospital Bonn, 53127 Bonn, Germany
[15]Lead contact
*Correspondence: mikael.simons@dzne.de
https://doi.org/10.1016/j.immuni.2024.07.001

SUMMARY

The reduced ability of the central nervous system to regenerate with increasing age limits functional recovery following demyelinating injury. Previous work has shown that myelin debris can overwhelm the metabolic capacity of microglia, thereby impeding tissue regeneration in aging, but the underlying mechanisms are unknown. In a model of demyelination, we found that a substantial number of genes that were not effectively activated in aged myeloid cells displayed epigenetic modifications associated with restricted chromatin accessibility. Ablation of two class I histone deacetylases in microglia was sufficient to restore the capacity of aged mice to remyelinate lesioned tissue. We used Bacillus Calmette-Guerin (BCG), a live-attenuated vaccine, to train the innate immune system and detected epigenetic reprogramming of brain-resident myeloid cells and functional restoration of myelin debris clearance and lesion recovery. Our results provide insight into aging-associated decline in myeloid function and how this decay can be prevented by innate immune reprogramming.

INTRODUCTION

Following primary demyelination in diseases such as multiple sclerosis (MS), a spontaneous regenerative process, called remyelination, is initiated, leading to the differentiation of oligodendrocyte progenitor cells (OPCs) into mature oligodendrocytes that generate new myelin sheaths around axons.[1–4] The repair process requires an injury-induced innate response, tailored toward the damaged tissue to facilitate its elimination from the lesion area.[5] Remyelination can occur in MS lesions, but with increasing age, it progressively becomes incomplete, ultimately resulting in failure for the majority of patients and lesions.[6–11] Thus, identifying the cause of this age-related decline and preventing it are key objectives in the field of regenerative medicine.

To clear the large quantities of myelin debris containing high levels of lipids, specifically cholesterol, microglia and monocyte-derived macrophages must produce specific transcriptional responses to facilitate myelin debris phagocytosis and lipid metabolism.[10,12–15] In lesions of aged rodents, not only is phagocytosis compromised but the degradation and metabolism of tissue debris is also hindered[7,10]; however, the understanding of the underlying reasons why microglia/macrophage responses become insufficient and even maladaptive in aging is incomplete. In particular, myelin-debris-derived cholesterol

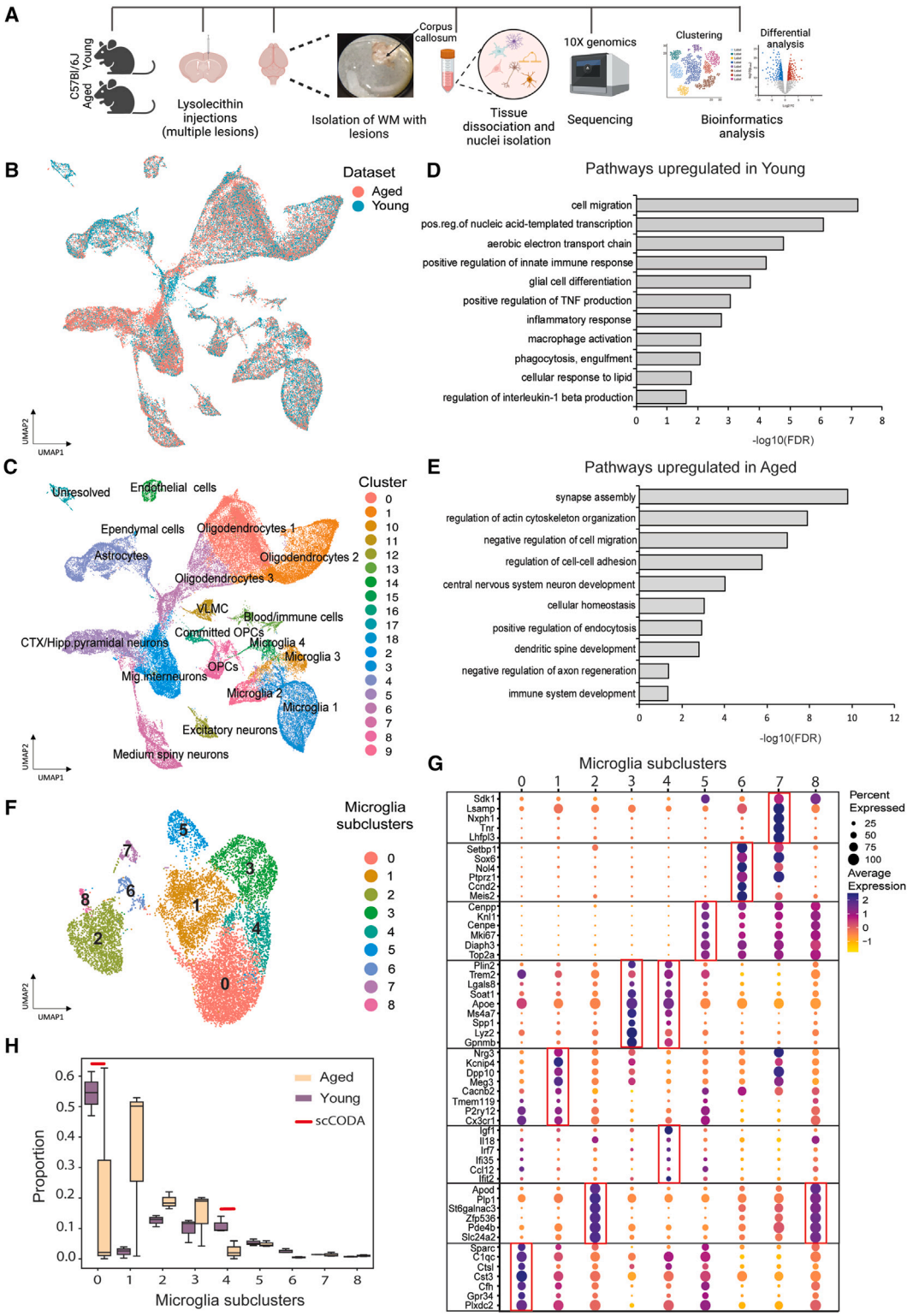

Figure 1. Single-nucleus RNA-seq identifies distinct cellular responses in young and aged white matter after demyelinating injury

(A) Schematic representation of the snRNA-seq experiment and downstream bioinformatic analyses.

(B) UMAP plot divided by total nuclei profiled in young (30,930) and aged (35,696) datasets.

(C) UMAP plots of all cell types identified in the snRNA-seq dataset, where dots correspond to individual nuclei profiled and where each cell type cluster is color coded, identifying 19 different clusters.

(legend continued on next page)

poses a challenge to aged phagocytes. Because cholesterol cannot be degraded and accumulation of free cholesterol is cytotoxic, phagocytes need to load cholesterol onto lipoprotein particles for its disposal into the extracellular space. Lipoprotein assembly is under the control of the liver X receptor (LXR) transcription factor, which form heterodimers with retinoid X receptor (RXR); together, they enhance the expression of apolipoprotein E (APOE), ATP binding cassette subfamily A member 1 (ABCA1), and ATP binding cassette subfamily G member 1 (ABCG1), which are essential for the so-called reverse cholesterol pathway.[16] However, aged rodents fail to induce the LXR/RXR pathway and consequently foamy microglia/macrophages with signs of cholesterol overloading accumulate in lesions, which impedes the regenerative responses of oligodendrocytes and their progenitors.[10,15,17] Aging itself is associated with low-grade inflammation, often referred to as "inflammaging,"[18] characterized by elevated expression of inflammatory markers in a subpopulation of microglia, in particular, within the white matter.[19] Thus, it is possible that upon aging, microglia become committed toward alternative inflammatory states and, as a result, lose their plasticity for pro-regenerative brain injury responses.

Here, we tested the hypothesis that age-related epigenetic changes contribute to attenuated responsiveness and to decreased reparative functions of microglia/macrophages in demyelinating lesions. Such epigenetic mechanisms, including DNA methylation and chromatin/histone modifications, are required to regulate transcriptional programs for microglia/macrophage activation.[20] Among those are histone deacetylases (HDACs) that, along with histone acetyl transferases (HATs), reversibly regulate the acetylation status of histones.[20]

In addition, we investigated whether innate immune training in aged mice could epigenetically reprogram—and thereby revitalize—microglial responses to reinstate reparative inflammation. Trained immunity is defined as a condition in which a stimulus can durably prime cells, in particular those of the myeloid lineage, to respond more strongly to future stimuli.[21–25] The concept of innate immune training was first introduced in microbiology, when several studies showed that myeloid cells could develop resistance to re-infection of the same or even unrelated pathogens in a response that is independent of adaptive immunity. Innate immune memory, often mediated by epigenetic reprogramming, can last for only a few months in circulating monocytes but can persist for at least 6 months in microglia, which are long-lived.[26,27] Here, we used Bacillus Calmette-Guerin (BCG), a live-attenuated vaccine strain of *Mycobacterium bovis*, to train the innate immune system.[28] BCG was developed against tuberculosis, but has been shown to also reduce morbidity and mortality in non-related infections and is even used as a non-specific immunotherapy in bladder cancer.[21,29] Given the cross-protection provided by BCG, we tested its efficiency and the underlying epigenetic mechanisms in training microglia toward pro-regenerative responses following demyelinating injury in aging. In conclusion, our data suggest that age-related epigenomic changes impair the regenerative functions of microglia, but innate immune training can reverse these changes and enhance their pro-regenerative abilities in demyelinating injuries.

RESULTS

snRNA-seq identifies differences in microglial responses in young and aged mice following demyelinating injury

Previous studies have demonstrated that young mice recover relatively rapidly from demyelinating injuries, while older mice experience inadequate microglial responses that hinder myelin debris and lipid removal.[7,30,31] In this study, we utilized mice aged 12 and 15 months, referred to as aged mice. To examine how microglia tailor their responses differently in young and aged mice following demyelinating injury, we used a toxin-induced model in which injections of lysolecithin (LPC) induce focal demyelinating lesions in the white matter of the brains of mice. In this model, microglia are the dominant myeloid cell population, as only a small number of monocyte-derived macrophages enter lesions from the periphery.[32–34] In lesioned animals, demyelination is complete within 4–7 days, followed by a repair process that reaches its maximum between 14 and 21 days post injection (dpi).[35] We induced two focal demyelinating lesions on each side of the corpus callosum of young (3 months) and aged (15 months) mice by LPC injections, then dissected white matter tracts, including the corpus callosum and medial lemniscus, from the brains of lesioned mice at 7 dpi for single-nucleus RNA sequencing (snRNA-seq) based on 10× Genomics (Figure 1A). After quality control and filtering, we obtained 35,696 and 30,930 single-nuclear transcriptomes from aged and young white matter tracts, respectively (Figures 1B and S1A–S1E). Cell type composition was analyzed using unsupervised uniform manifold approximation and projection (UMAP) analysis and Louvain clustering algorithm to the batch-corrected transcriptomic datasets. The cell type identities were confirmed by the expression of canonical cell type marker genes, which identified 19 different clusters in both young and aged datasets. Microglia were distributed in four different clusters composed of a total of 5,792 and 6,093 nuclei for aged and young white matter tracts, respectively (Figure 1C; Table S1). The microglial clusters shared the injury- or disease-associated response signature previously described in various disease models, with relatively higher average expression in

(D and E) Gene Ontology (GO) term enrichment analysis depicting ten terms for biological process (D) upregulated in young and (E) upregulated in aged microglial clusters using Fisher's exact test and Benjamini-Hochberg FDR correction.

(F) UMAP visualization of microglial subclusters obtained after reclustering the four clusters of microglia in which dots correspond to individual nuclei profiled with snRNA-seq.

(G) Dot plot of average expression of top differentially expressed genes in each microglia subcluster.

(H) Boxplots of cluster proportions in each subcluster of microglia per sample ($n = 3$) for both young and aged conditions, respectively. The central line denotes the median, boxes represent the IQR, and whiskers show the distribution. Significant results (scCODA) are indicated with red bars, FDR < 0.05 ($n = 3$ biological replicates per condition were used).

See also Figures S1–S3 and Tables S1 and S2.

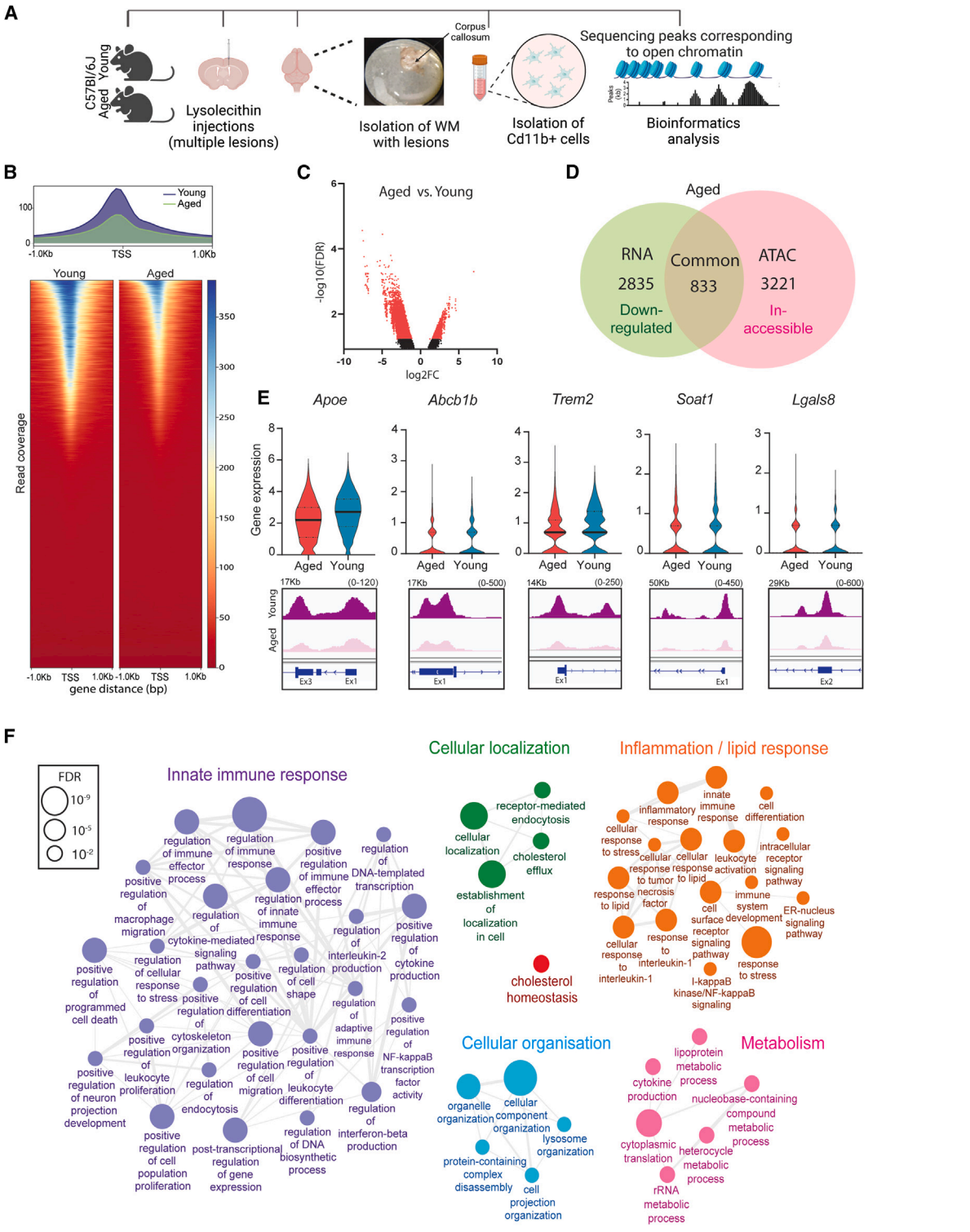

Figure 2. Epigenomic analysis reveals differences in young and aged microglia/macrophages after demyelinating injury

(A) Schematic representation of the ATAC-seq experiment on CD11b^{+} cells isolated from lesioned white matter (WM) of young and aged mice.

(B) Plot profile depicting the average enrichment around transcription start site (TSS) and heatmap summarizing the coverage of genomic reads, with a color code from red (no coverage) to blue (maximum coverage), from −1 to +1 kb around the TSS between young and aged microglia.

(C) Volcano plot of differentially accessible regions in aged compared with young microglia, FDR < 0.05.

(D) Venn diagram indicating common genes between snRNA and ATAC-seq datasets that are downregulated in aged microglia due to reduced accessibility.

(legend continued on next page)

clusters 1 and 2 microglia (Figure S2A).[34,36–40] Gene ontology analysis revealed that microglia in young mice were enriched for pathways such as cell migration, positive regulation of innate immune response, glial cell differentiation, macrophage activation, and cellular response to lipids. Microglia in aged mice, in contrast, were enriched for pathways including synapse assembly, regulation of cell-cell adhesion, central nervous system (CNS) neuron development and cellular homeostasis (false discovery rate [FDR] < 0.05) (Figures 1D and 1E). To obtain higher resolution of the distinct clusters, we re-clustered microglia from lesions of young and aged mice, resulting in the identification of nine distinct clusters (Figure 1F). Differential marker gene expression identified distinct expression of genes, thereby segregating the clusters. Cluster 0 was characterized by increased expression of genes involved in complement activation, cell activation, and immune response (*Sparc*, *C1qc*, *Ctsl*, *Cst3*, *Cfh*, *Gpr34*, and *Plxdc2*). Cluster 1 was associated with homeostatic processes and was high in genes such as (*Tmem119*, *P2ry12*, and *Cx3cr1)*. Clusters 3 and 4 displayed upregulation of lipid metabolism (*Plin2*, *Trem2*, *Lgals8*, *Soat1*, *Apoe*, and *Gpnmb*), with cluster 4 showing an additional upregulation of interferon signaling (*Irf7*, *Ifi35*, *Ccl12*, and *Ifit2*), whereas cluster 5 was marked by genes involved in proliferation (*Top2a*, *Diaph3*, *Knl1*, and *Mki67*) (Figure 1G; Table S2). Using single-cell differential composition analysis (scCODA), which takes account of the compositional changes in the scRNA-seq data and reliably controls for false discoveries, we identified microglial clusters 0 and 4 to be significantly higher in young compared with aged mice (Figure 1H). Cluster 0 expressed genes involved in pathways such as microglial cell activation, neuroinflammation, and responses to lipids, whereas cluster 4 expressed genes involved in pathways such as phagocytosis, positive regulation of innate immune response, and regulation of cytokine expression (Figure S2C). In addition, we also found differences in the expression of genes that are functionally associated with lipid metabolism, innate immune responses and activation in young mice compared with aged ones in clusters 0 and 4 (Figures S3A–S3S). Hence, the data suggest that microglia in aged mice display inadequate transcriptional responses related to innate immunity and lipid metabolism.

Aged myeloid cells display epigenetic modifications associated with restricted chromatin accessibility

Gene expression is highly regulated through the remodeling of chromatin, which occurs by transcription factors recruiting coactivator complexes that are capable of modifying histone tails and remodeling nucleosomes.[41,42] This repositioning of the nucleosomes around promoters and enhancers makes chromatin accessible to other transcription factors and RNA polymerase II near promoters, thereby regulating active transcription. We hypothesized that the impaired function of microglia/macrophages in aging following demyelinating injury might be due to chromatin inaccessibility, preventing the transcriptional induction of genes involved in pathways such as the innate immune response and lipid metabolism. Thus, we performed bulk assay for transposase-accessible chromatin sequencing (ATAC-seq) on CD11b$^+$ cells isolated from the white matter of young and aged mice at 4 dpi (Figure 2A). Fragment length distribution of samples revealed distinct peaks at around 50, 200, 400, and 600 bp, respectively, ensuring the quality and downstream analysis. In addition, we confirmed using fluorescence activated cell sorting (FACS) that 94%–96% CD11b$^+$ cells were microglia in lesioned tissue of young and aged mice, respectively (STAR Methods, Figures S1F, S1G, and S4A). We observed a higher landscape of open chromatin regions around ±1 kb of transcription start site (TSS) in young mice compared with aged. Differential analysis revealed fewer differentially accessible regions in aged compared with young mice (Figures 2B and 2C). To determine whether altered transcription in aged microglia/macrophages is due to decreased chromatin accessibility, we compared the genes that were downregulated in aged microglia in snRNA-seq with the regions that were inaccessible in aged microglia/macrophages identified by ATAC-seq. Our analysis revealed the presence of 833 common genes in both datasets, suggesting that approximately 30% of genes exhibiting low transcriptional activity following demyelinating injury in aged microglia were correlated with chromatin inaccessibility (Figure 2D). Enrichment analysis of shared genes uncovered innate immune response, lipid response, cellular localization, organization, and metabolism, as the major clusters of pathways downregulated in aged mice due to reduced accessibility (FDR < 0.05) (Figures 2E, 2F, and S2E). We performed motif enrichment analysis using Homer on shared genes and discovered the following motifs to be underrepresented in aged microglia: RAR: RXR and Nr5a2, both implicated in lipid metabolism and cholesterol transport; ZEB1, E2A near PU.1 and Runx1with functions in immune response, microglia proliferation, and differentiation (Figure S2D). Together, these data suggest that deficient microglial activation and myelin lipid clearance in aged mice following demyelinating injury could be attributed to inadequate transcription of genes due to reduced accessibility of chromatin around promoters.

Immune training with BCG alters the microglial chromatin landscape of aged mice

To instruct aged microglia/macrophages in generating a pro-regenerative response following demyelinating injury, we applied a vaccine-based innate immune training protocol. We administered the BCG vaccine, typically utilized to combat tuberculosis but also known for its ability to reprogram the innate immune cells epigenetically by altering the chromatin marks H3K27ac and H3K4me3.[43,44] To determine whether peripheral application of BCG can alter the chromatin landscape of microglia/macrophages within the brain, we analyzed CD11b$^+$ cells isolated from mice treated with BCG or saline for the following histone marks, H3K4me3 and H3K27ac, using chromatin

(E) Violin plots indicating (log-normalized) expression of expressed genes involved in lipid metabolism in all microglial clusters, along with accessibility profile showing the coverage of genes in the promoter region. The first exon for each gene is indicated below, FDR < 0.05.
(F) Enrichment map of biological pathways downregulated in aged mice due to reduced accessibility, using Fisher's exact test and Benjamini-Hochberg FDR correction (n = 2 biological replicates per condition).
See also Figures S1 and S2.

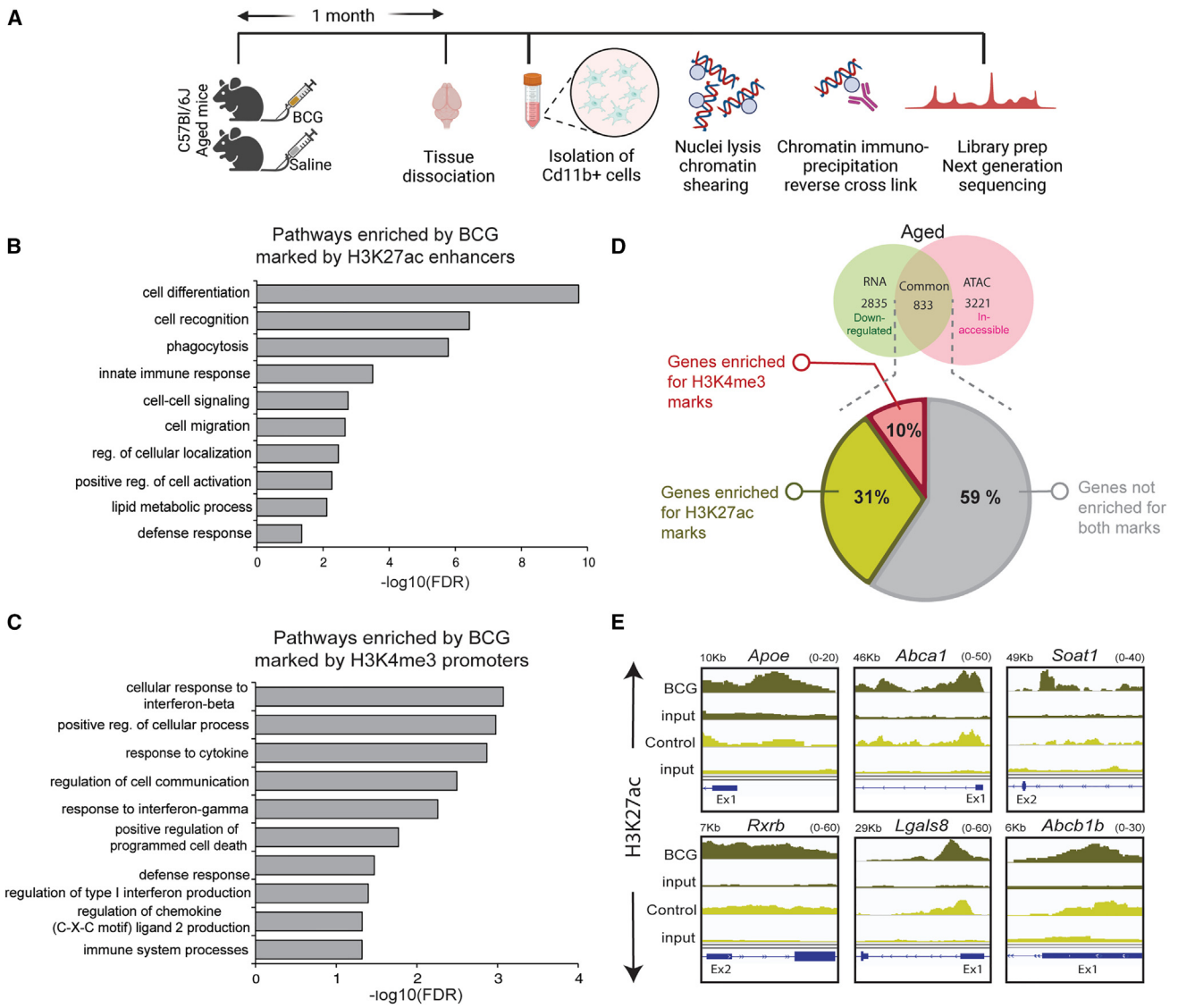

Figure 3. ChIP-seq reveals enrichment of H3K27ac and H3K4me3 epigenetic marks in microglia/macrophages of BCG-treated aged mice

(A) Schematic representation of the ChIP-seq experiment on CD11b$^+$ cells isolated from aged mice treated with BCG or saline.

(B and C) GO term enrichment analysis depicting ten terms for biological process (B) enriched for H3K27ac marks and (C) enriched for H3K4me3 marks in aged mice treated with BCG using Fisher's exact test and Benjamini-Hochberg FDR correction.

(D) Pie chart representing the percentage of genes enriched for H3K27ac and H3K4me3 marks after BCG treatment out of the common set of genes in snRNA and ATAC-seq.

(E) Coverage plots of H3K27ac marks and input for the differentially regulated genes in control (saline) and BCG-treated mice. The exon for each gene is indicated below, FDR < 0.05 (n = 2 independent replicates per condition for each histone mark. Each replicate was a pool of 3 animals).

See also Figures S1 and S4.

immunoprecipitation DNA sequencing (ChIP-seq) (Figures 3A and S4A–S4C). We found greater enrichment of H3K27ac and H3K4me3 marks in CD11b$^+$ cells isolated from BCG-treated compared with control mice (Figures S1H and S4E). The genes enriched for the H3K27ac mark were involved in pathways including differentiation, migration, innate immune response, and lipid metabolism, while the genes enriched for H3K4me3 were involved in inflammation and interferon response (Figures 3B and 3C). We performed motif enrichment analysis on differentially expressed enriched regions for H3K27ac and H3K4me3 using Homer (Figure S4D). If these histone marks induced by BCG are beneficial in microglial reprogramming toward pro-regenerative behaviors, they should appear at locations that coincide with genes exhibiting inaccessible chromatin regions in aged microglia/macrophages. Thus, we conducted a comparative analysis between the shared set of genes that were poorly transcribed and inaccessible in aged microglia following demyelinating injury with those displaying BCG-induced changes for either H3K27ac or H3K4me3 histone marks. We found that 31% of the shared set of genes were also enriched for H3K27ac marks, including those

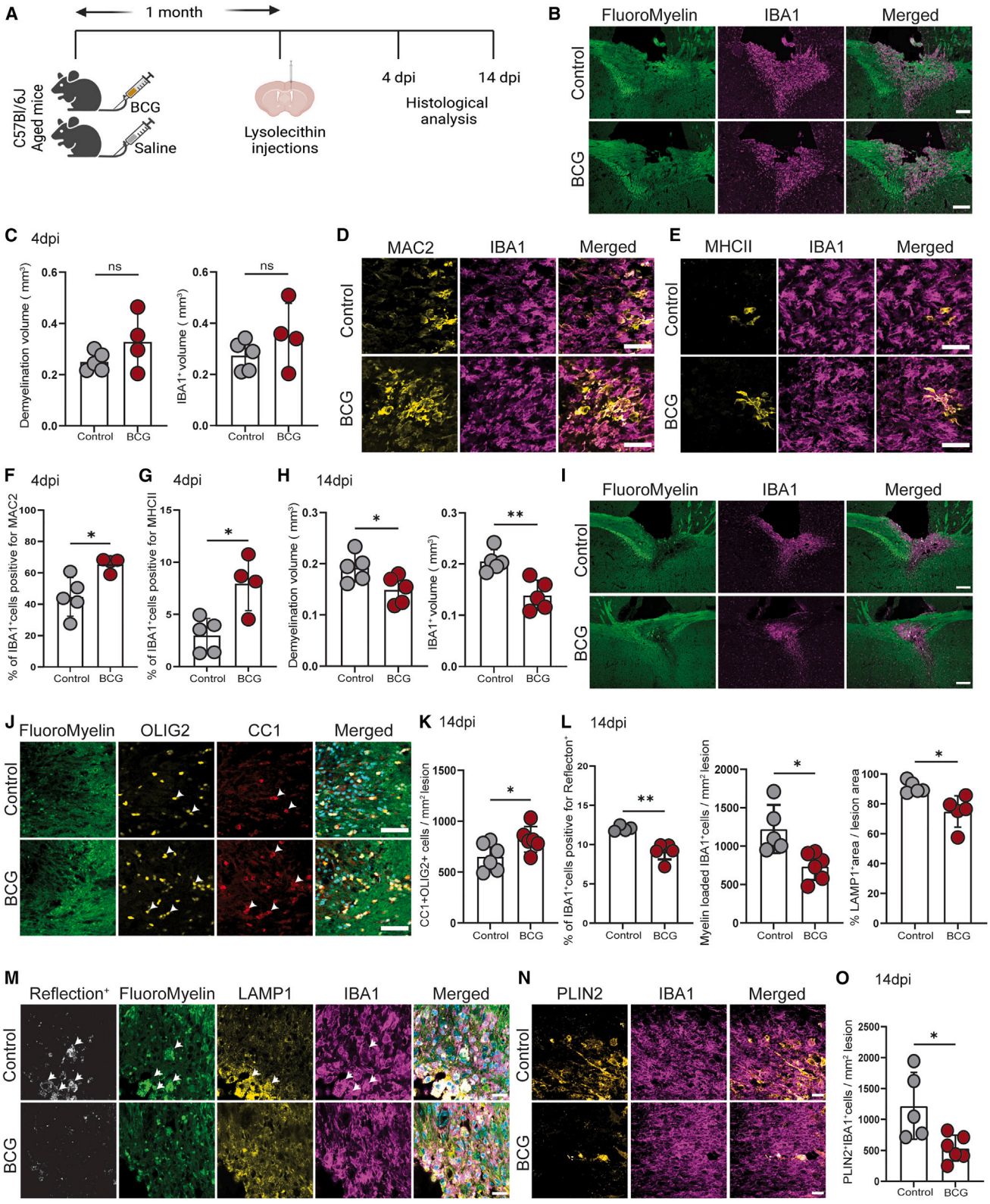

Figure 4. BCG immunization promotes lesion recovery after demyelinating injury in aged mice

(A) Schematic representation of BCG treatment and experimental timeline in aged mice.

(B) Images of corpus callosum lesions in aged (12 months) mice treated with BCG or saline at 4 dpi. Scale bars, 200 μm.

(C) Quantification of lesion volume and IBA1⁺ volume in aged (12 months) mice treated with BCG or saline at 4 dpi.

(legend continued on next page)

involved in lipid metabolism (*Apoe*, *Abca1*, *Soat1*, and RXR beta [*Rxrb*]) and innate immune response (*Nod1, Irgm1*, *Ifit2*, *Tlr7*, *Itga6*, *Irf2*, and *Ifitm10*). 10% of the shared set of genes were enriched for H3K4me3 marks, which were mostly involved in inflammation and interferon response (*Nod1*, *Irgm1*, *Ifi35*, *Cd48*, *Itga6*, *Irf2*, and *H2-Q4*) (FDR < 0.05) (Figures 3D, 3E, S4F, and S4G). Taken together, our data indicate that BCG-induced immune training can alter the chromatin landscape in microglia for H3K27ac and H3K4me3 histone marks, and some of these occur at sites that coincide with the set of genes that are poorly transcribed after demyelinating injury.

BCG vaccination promotes recovery from lesions after demyelinating injury

To examine the role of BCG-induced training in CNS lesion recovery, we applied BCG or saline intravenously 1 month prior to lesion induction in aged mice and analyzed lesions at 4 and 14 dpi (Figure 4A). We measured the size of lesions with a fluorescent myelin stain (FluoroMyelin) and quantified phagocytes using anti-IBA1 antibodies. At 4 dpi, demyelinating lesion volumes were of a similar size in BCG- and saline-treated mice, and a comparable area of the lesions was occupied by IBA1$^+$ cells, showing that lesion formation was unaltered (Figures 4B and 4C). We used immunohistochemistry to examine phagocyte reactivity at 4 dpi in BCG-treated mice and controls, and found a higher percentage of MAC2$^+$IBA1$^+$ and MHCII$^+$IBA1$^+$ cells in the lesions of BCG-treated compared with control mice (Figures 4D–4G). Because previous studies have shown that BCG-induced training can increase TNF-α and IL1β in monocytes and macrophages,[43] we performed *Tnf* and *Il1β* RNA *in situ* hybridization (RNAscope multiplex fluorescent assay) and detected a higher percentage of IBA1$^+$ cells positive for *Tnf*$^+$*Il1β*$^+$ mRNA particles in 4 dpi lesions of BCG-treated mice (Figures S5A and S5B). To determine possible differences in lesion recovery, we assessed the size of lesions at 14 dpi, a time point when the repair process reaches its peak, and found smaller lesion volumes in BCG-treated compared with control mice (Figures 4H and 4I). Moreover, assessment of oligodendrocytes using antibodies against anti-adenomatous polyposis coli (APC), clone CC1, and BCAS1 revealed a higher percentage of mature CC1$^+$ as well as pre- and actively myelinating BCAS1$^+$ oligodendrocytes in 14 dpi lesions of BCG-treated mice (Figures 4J, 4K, S5C, and S5D). Previous studies have detected sustained immune infiltration in lesions of aged compared with young mice. Therefore, we measured the density of IBA1$^+$ cells in lesions at 14 dpi, and the results showed a decrease due to BCG vaccination (Figures 4H and 4I). Following that, we examined how BCG vaccination affects the ability of microglia/macrophages to clear myelin debris and process lipids in lesions at 14 dpi. We measured the amount of IBA1$^+$LAMP1$^+$ cells that co-localized with FluoroMyelin and observed a decrease in myelin-debris accumulation within phagocyte lysosomes in mice that received BCG treatment. Quantification of lipid droplets using PLIN2 as a marker revealed fewer PLIN2$^+$IBA1$^+$ microglia in BCG-treated mice. Moreover, by a combination of laser reflection and fluorescence confocal microscopy (reflection microscopy) we detected a reduction in reflection-positive material (mostly cholesterol crystals/lipid droplets) in lesions of BCG-treated mice (Figures 4L–4O). We also examined the effect of BCG on lesion recovery and IBA1$^+$ cell density in young mice and did not observe any significant differences (Figures S5E and S5F). Together, these results provide evidence that BCG vaccination improves lesion recovery after demyelinating injury in aged mice.

To determine possible differences in transcriptional responses following BCG treatment, we conducted transcriptomic analysis on lesioned and unlesioned white matter tracts obtained from the brains of mice treated with either BCG or saline. Samples clustered into their respective experimental groups, as shown by principal-component analysis (PCA) (Figures 5A and S6A). To assess the differences between the two groups, we performed differential expression analysis and gene ontology analysis, which identified lipid metabolism, chromatin modification, aerobic respiration, and cellular localization as the key differentially regulated pathways in the lesions of BCG-treated mice compared with control (FDR < 0.05) (Figures S6B–S6D). Among the differentially expressed genes upregulated in lesions of BCG-treated mice were two lipid-sensing nuclear receptors, *Nr1h2* (LXR-A) and *Rxrb*, previously implicated in remyelination.[10,17] Because the reverse cholesterol pathway with *Abca1* and *Abcg1* as key molecules is under the control of these nuclear receptors,[45] we analyzed *Nr1h2, Abca1*, and *Abcg1* expression using RNA *in situ* hybridization and found higher expression in microglia/macrophages of BCG compared with control (Figures S6C and S6E–S6I). Furthermore, genes involved in histone acetylation and deacetylation were shown to be potentially differentially expressed in the lesions of BCG-treated mice (Figures S6C and S6J). In unlesioned white matter, differential expression and

(D and E) Images of (D) MAC2$^+$IBA1$^+$ and (E) MHCII$^+$IBA1$^+$ cells in the demyelinated lesions at 4 dpi. Scale bars, 50 μm.
(F and G) Quantification of the percentage of (F) MAC2$^+$IBA1$^+$ and (G) MHCII$^+$IBA1$^+$ cells over IBA1$^+$ cells in the demyelinated lesion at 4 dpi.
(H) Quantification of lesion volume and IBA1$^+$ volume in aged (12 months) mice treated with BCG or saline at 14 dpi.
(I) Images of corpus callosum lesions in aged (12 months) mice treated with BCG or saline at 14 dpi. Scale bars, 200 μm.
(J) Images of the demyelinated lesions in the corpus callosum at 14 dpi exemplifying the numbers of CC1$^+$OLIG2$^+$ cells at the demyelination/remyelination edge. White arrows indicate CC1$^+$OLIG2$^+$ cells. Scale bars, 50 μm.
(K) Quantification of CC1$^+$OLIG2$^+$ cells per mm^2 of lesion at 14 dpi.
(L) Quantification of the percentage of IBA1$^+$ cells positive for reflection, myelin loaded (FluoroMyelin$^+$) IBA1$^+$ cells per mm^2 of lesion, and percentage of lesion area occupied by LAMP1$^+$ signal at 14 dpi.
(M) Images demonstrating reflection microscopy and accumulation of myelin debris in LAMP1$^+$IBA1$^+$ cells in demyelinated lesions at 14 dpi. White arrows point to reflection$^+$ myelin-debris accumulation within LAMP1$^+$IBA1$^+$ cells. Scale bars, 50 μm.
(N) Images of demyelinated lesions at 14 dpi demonstrating PLIN2$^+$ signal within IBA1$^+$ cells. Scale bars, 50 μm.
(O) Quantification of PLIN2$^+$IBA1$^+$cells per mm^2 of lesion at 14 dpi.
All data are mean ± SD; *$p < 0.05$, **$p < 0.001$, ***$p < 0.0001$; ns, not significant; two-tailed Welch's t test or Mann-Whitney test (C, F–H, K, L, and O), *n* numbers are indicated in the figure, each dot represents one mouse.
See also Figure S5.

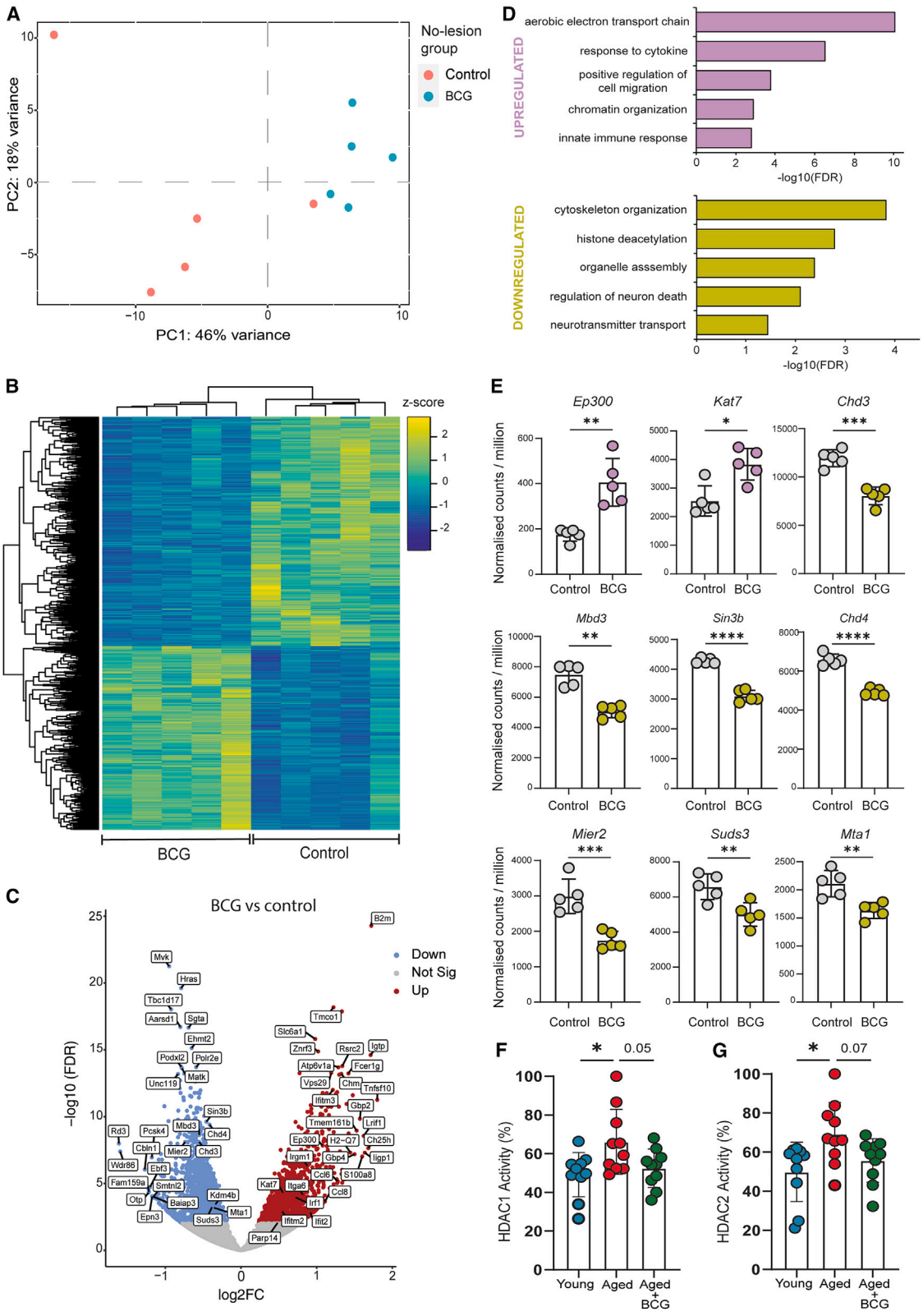

Figure 5. BCG treatment alters the transcriptome of cells in unlesioned white matter

(A) Principal-component analysis (PCA) of RNA-seq normalized read counts from BCG and control group, where each replicate is plotted as an individual data point.

(legend continued on next page)

gene ontology analysis identified upregulated pathways, such as aerobic electron transport chain, cell migration, chromatin organization, and innate immune response, while downregulated pathways included histone deacetylation, organelle assembly, and regulation of neuron death (FDR < 0.05) (Figures 5B–5D). Additionally, genes related to histone acetylation and deacetylation showed differential expression in unlesioned samples of BCG-treated mice. Specifically, we observed upregulation of genes involved in histone acetylation (*Kat7* and *Ep300*), and downregulation of genes known to regulate the activity of HDAC (HDAC 1 and 2) by forming a core repressor complex (*Sin3b*, *Chd4*, *Mbd3*, *Mier2*, *Mta1*, *Chd3*, and *Suds3*)[46] (Figure 5E).

Genetic ablation of HDAC1 and HDAC2 from aged microglia improves lesion recovery

HDACs are enzymes that modify histones and, together with HATs, control the acetylation status of histones, thereby affecting gene expression, with two class I HDACs (HDAC 1 and 2) having previously been shown to be of functional importance in microglia.[47] To determine the involvement of HDAC1 and HDAC2, we isolated CD11b$^+$ cells from young, aged, and aged mice treated with BCG, and measured HDAC1 and 2 activity in cell extracts using a fluorometric assay. Our analysis revealed that the activity of HDAC1 and HDAC2 was significantly higher in CD11b$^+$ cells isolated from aged compared with young mice (Figures 5F and 5G). HDAC1 and HDAC2 activities were reduced (but only with a trend toward significance) in CD11b$^+$ cells from BCG-treated aged mice relative to untreated aged mice (Figures 5F and 5G). These results prompted us to explore the role of HDACs as possible mediators in epigenetic reprogramming. To determine whether the depletion of HDAC1/2 modifies pro-regenerative microglial responses in aged mice, we generated tamoxifen-inducible mice that lack *Hdac1,2* in microglia. This was achieved by crossing *Cx3cr1*^{CreERT2} with mice carrying floxed alleles for *Hdac1* and *Hdac2* to obtain *Cx3cr1*^{CreERT2} *Hdac1*$^{fl/fl}$ *Hdac2*$^{fl/fl}$ (HDAC1/2 knockout [KO])[47] (Figure 6A). Because microglia are long-living cells compared with circulating monocytes, mainly microglia in the CNS parenchyma are targeted.[48] First, we confirmed the ablation of *Hdac1* and *Hdac2* transcripts in microglia/macrophages purified from the brain of HDAC1/2 KO and control mice by RT-qPCR (Figure 6B). Next, we injected LPC into the corpus callosum of aged HDAC1/2 KO and the corresponding control mice (*Hdac1*$^{fl/fl}$*Hdac2*$^{fl/fl}$ lacking *Cx3cr1*^{CreERT2} but with tamoxifen injection) to induce demyelinating lesions and examined mice at 4 and 14 dpi to identify potential changes in lesion formation and recovery. At 4 dpi, no differences in lesion volume or in IBA1$^+$ cell density were identified within lesions (Figures S5G and S5H). However, we detected higher percentages of MAC2$^+$IBA1$^+$ and MHCII$^+$IBA1$^+$ cells in lesions of HDAC1/2 KO (Figures 6C–6F). When lesions were analyzed at 14 dpi, we observed smaller lesion volumes, as determined by FluoroMyelin staining and a decrease in IBA1$^+$ cell density, pointing to enhanced lesion recovery in HDAC1/2 KO compared with control mice (Figures 6G and 6H). Similar results were obtained when 15-month-old HDAC1/2 KO and control mice were used (Figures S5I and S5J). Because our control mice express *Hdac1*$^{fl/fl}$*Hdac2*$^{fl/fl}$, but lack *Cx3cr1*^{creERT}, we used *Cx3cr1*$^{creERT/het}$ *Hdac1*$^{wt/wt}$ *Hdac2*$^{wt/wt}$ as an additional control. Using these control mice, we were able to validate the effect of HDAC1 and HDAC2 ablation in enhancing lesion recovery and in resolving IBA1$^+$ cells from 14 dpi lesions (Figures S5K and S5L). Next, we quantified oligodendrocyte density using antibodies against APC, clone CC1, which revealed a higher number of mature CC1$^+$ oligodendrocytes in lesions of HDAC1,2 KO at 14 dpi (Figures 6I and 6J). In addition, FluoroMyelin stain and antibodies against IBA1 detected less accumulation of myelin debris within LAMP1$^+$IBA1$^+$ cells. Reflection microscopy identified decreased reflection$^+$ material in IBA1$^+$ cells and using antibodies against the lipid droplet marker, PLIN2, fewer PLIN2$^+$ IBA1$^+$ cells were observed in lesions at 14 dpi of HDAC1/2 KO compared with control (Figures 6K–6N). In addition, we performed RNA *in situ* labeling and found higher expression of *Abca1* and *Abcg1* in microglia/macrophages of HDAC1/2 KO compared with control (Figures 6O and 6P). Together, these data provide evidence that *Hdac1* and *Hdac2* ablation from microglia/macrophages improves lesion recovery after demyelinating injury in aged mice.

Next, we aimed to determine the role of HDAC1 and HDAC2 in microglia/macrophages concerning the BCG-induced immune training effect. We induced the KO by tamoxifen administration to aged HDAC1/2 KO or control mice, administered BCG or saline, and 1 month later, we injected LPC into the corpus callosum to induce demyelinating lesions and examined mice at 14 dpi to identify potential changes in lesion recovery (Figure 7A). We found that BCG treatment enhanced lesion recovery, as determined by FluoroMyelin staining, and decreased the density of IBA1$^+$ cells in lesions as compared with saline-treated control mice (*Hdac1*$^{fl/fl}$*Hdac2*$^{fl/fl}$ with tamoxifen injection) (Figures 7B, 7D, and 7E). When HDAC1/2 KO mice were analyzed, we found no differences in lesion volume and IBA1$^+$ cell density in 14 dpi lesions when BCG and saline-treated animals were compared (Figures 7B, 7D, and 7E). Together, these results show that BCG-induced immune training is abolished by the ablation of HDAC1/2 from microglia/macrophages.

(B) Heatmap of differentially expressed genes over samples of BCG and control indicating *Z* scores.
(C) Volcano plot of differentially expressed genes in BCG-treated mice compared with control mice, FDR < 0.05.
(D) Gene Ontology (GO) term enrichment analysis depicting five terms for biological processes upregulated and downregulated in unlesioned corpus callosum of BCG-treated aged mice using Fisher's exact test and Benjamini-Hochberg FDR correction.
(E) Bar plots designating normalized counts per million (CPM) of upregulated and downregulated differentially expressed genes in no-lesion group involved in histone acetylation and deacetylation, respectively, FDR < 0.05.
(F) Quantification of percentage of *Hdac1* activity in CD11b$^+$ cells isolated from young mice, aged mice, and aged mice treated with BCG, respectively.
(G) Quantification of percentage of *Hdac2* activity in CD11b$^+$ cells isolated from young mice, aged mice, and aged mice treated with BCG, respectively.
All data are mean ± SD; *p < 0.05, **p < 0.001, ***p < 0.0001, ****p < 0.00001; ns, not significant.
One-way ANOVA with Bonferroni multiple comparison test (F and G) and two-tailed Student's t test (E), *n* numbers are indicated in the figure, each dot represents one mouse.
See also Figure S6 and Table S3.

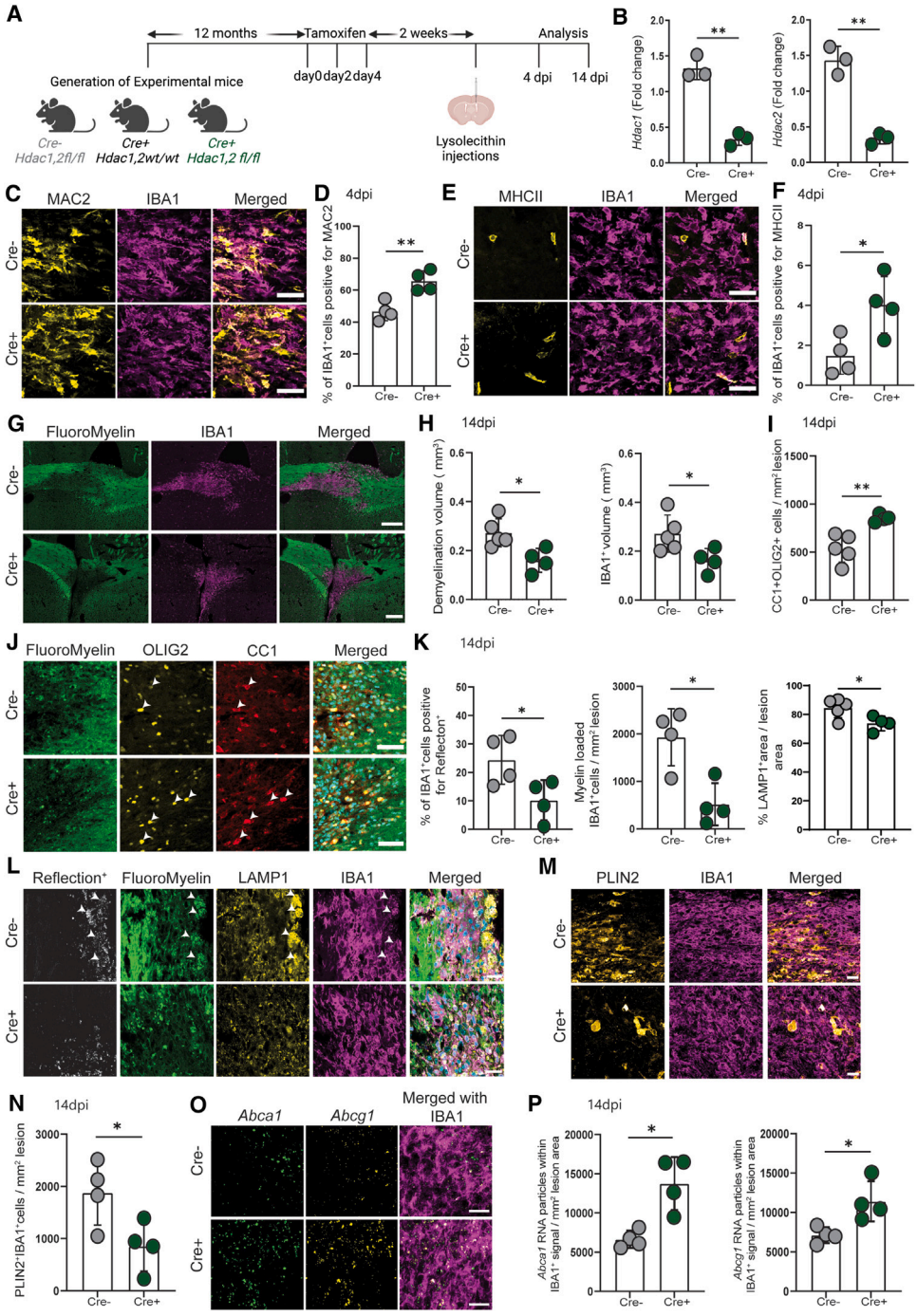

Figure 6. HDAC1/2 depletion in microglia improves remyelination in aged mice

(A) Schematic representation of experimental paradigm in *Cx3cr1*$^{creERT/het}$*Hdac1*$^{fl/fl}$*Hdac2*$^{fl/fl}$ aged mice.

(B) Quantitative PCR analysis of *Hdac1* and *Hdac2* in CD11b^{+} cells isolated from Cre− and Cre+ mice 2 weeks after tamoxifen induction.

(C) Images of MAC2^{+}IBA1^{+} cells in the demyelinated lesions at 4 dpi. Scale bars, 50 μm.

(D) Quantification of the percentage of MAC2^{+}IBA1^{+} cells over IBA1^{+} cells in the demyelinated lesion at 4 dpi.

(E) Images of MHCII^{+}IBA1^{+} cells in the demyelinated lesions at 4 dpi. Scale bars, 50 μm.

(F) Quantification of the percentage of MHCII^{+}IBA1^{+} cells over IBA1^{+} cells in the demyelinated lesion at 4 dpi.

(G) Images of corpus callosum lesions in aged (12 months) Cre− (control) and Cre+ (knockout) mice at 14 dpi. Scale bars, 200 μm.

(H) Quantification of lesion volume and IBA1^{+} volume in aged (12 months) Cre− (control) and Cre+ (knockout) mice at 14 dpi.

(I) Quantification of CC1^{+}OLIG2^{+} cells per mm^{2} of lesion at 14 dpi.

(legend continued on next page)

Subsequently, we analyzed a set of 18 genes selected for their decreased expression and reduced accessibility in aged microglia within lesions, and their enrichment with H3K27ac and H3K4me3 marks subsequent to BCG treatment. Lesions were isolated at 7 dpi from 12-month-old *Cx3cr1*^{CreERT2}*Hdac1*$^{fl/fl}$ *Hdac2*$^{fl/fl}$ mice and control mice, as well as from mice treated with either BCG or saline, and RT-qPCR was performed to assess transcript levels. Notably, we observed that a subset of genes (*Apoe*, *Abca1*, *Abcg1*, *Lamp2*, *B2m*, *Parp14*, *Ctsb*, *Nod1*, *Irgm1*, and *Irf7*) associated with lipid metabolism and the innate immune response exhibited significantly higher expression following BCG treatment. HDAC1/2 KO induced a very similar set of genes in lesions (Figures 7F–7J). We conducted RNA *in situ* hybridization together with immunofluorescence staining, employing antibodies against IBA1 to visualize the expression of these genes at the individual cell level within lesions. Our RNA *in situ* hybridization unveiled elevated expression of *Abca1*, *Abcg1*, *Irf7*, *Irgm1*, *Parp14*, and *Lamp2* in IBA1$^+$ cells of HDAC1/2 KO mice compared with controls. A similar upregulation was also noted following BCG vaccination. When HDAC1/2 KO mice were administered BCG treatment, no additional increase in gene expression was observed (Figures S7A–S7L). To explore the potential correlation between epigenetic alterations and gene expression changes, we conducted ChIP-qPCR analyses for H3K27ac marks on CD11b$^+$ cells isolated from young, aged, and aged HADC1/2 KO mice. We focused on H3K27ac marks because they were found to be enriched in lipid and innate pathways in microglia following BCG vaccination in aged mice. We found significant enrichment of H3K27ac on several genes (*Abca1*, *Abcg1*, *Lgals8*, *B2m*, *Ctsb*, *Irf7*, *Irgm1*, *Nod1*, and *Parp14*) in CD11b$^+$ cells isolated from HDAC1/2 KO mice compared with controls. There was also an enrichment of H3K27ac at these genes in microglia isolated from young compared with aged mice (Figures S7M–S7P). Collectively, these results demonstrate that both BCG-induced immune training and HDAC1/2 KO induce a related set of genes associated with lipid metabolism and innate immune response in microglia within demyelinating lesions.

DISCUSSION

Age-associated decline in regeneration capacity limits the re-establishment of nervous system functionality after demyelinating injury.[1] Here, we reveal an altered transcriptional response of microglia to demyelinating damage in young and aged mice, with the largest differences in genes related to immune function and lipid metabolism. By assessing genome-wide chromatin accessibility, we found that a relatively large fraction of the genes had epigenetic changes associated with chromatin inaccessibility. Using KO of HDAC1/2 in microglia to increase histone acetylation and to enhance chromatin accessibility, we were able to restore microglial function and improve lesion recovery in aged mice. Furthermore, by applying a classical model of innate immune training, myelin repair was enhanced in the aging nervous system. Together, our data support the concept of age-related epigenomic alterations as one underlying factor for poor repair capacity of the aging CNS. Our results seem, at first glance unexpected, as previous data have convincingly shown that microglia of the aged brain are characterized by an elevated inflammatory profile, which is associated with a "sensitized" or "primed" phenotype.[49] Such primed microglia respond much more strongly to a secondary inflammatory stimulus.[50] For example, inflammatory challenge by peripheral injection of lipopolysaccharides generates an exaggerated and detrimental immune response by microglia in the aged brain and in mouse models of neurodegenerative disease.[27,51–53] Thus, aging cannot be equated with unresponsive microglia. Instead, we propose that aging creates a condition of microglial rigidity in which they lose their ability to mount a precisely adjusted injury response. Microglia possess an extensive array of sensors located on the cell surface as well as within the cytosol and nucleus, allowing them to identify damaged tissue and coordinate a response tailored to the specific type of injury that has occurred.[54–57] In demyelinating lesions rich in cholesterol and fatty acids from myelin debris, aged microglia exhibit poor activation of the transcriptional responses necessary for debris clearance, which is regulated by the nuclear lipid-sensing LXR/RXR pathway.[10] We showed that deletion of HDAC1/2 in microglia restored pro-regenerative lipid clearance function, suggesting that epigenetic alterations, and in particular histone acetylation levels, contribute to poor responsiveness of microglia toward demyelinating injury in aging. Most likely, the modulation of these specific gene expression patterns by HDACs is due to the action of transcriptional regulators that bind specific DNA sequences. HDAC1 and 2 are recruited to target genes via association with transcriptional complexes (e.g., Sin3 complex, NuRD complex, and Co-REST complex),[46] but how this occurs in microglia is not well known.

(J) Images of the demyelinated lesions in the corpus callosum at 14 dpi exemplifying the numbers of CC1$^+$OLIG2$^+$ cells at the demyelination-remyelination edge. White arrows indicate CC1$^+$OLIG2$^+$ cells. Scale bars, 50 μm.
(K) Quantification of the percentage of IBA1$^+$ cells positive for reflection, myelin loaded (FluoroMyelin$^+$) IBA1$^+$ cells per mm^2 of lesion and percentage of lesion area occupied by LAMP1$^+$ signal at 14 dpi.
(L) Images demonstrating reflection microscopy and accumulation of myelin debris in LAMP1$^+$IBA1$^+$ cells in demyelinated lesions at 14 dpi. White arrows point to reflection$^+$ myelin-debris accumulation within LAMP1$^+$IBA1$^+$ cells. Scale bars, 50 μm.
(M) Images of demyelinated lesions at 14 dpi demonstrating PLIN2$^+$ signal within IBA1$^+$ cells. Scale bars, 50 μm.
(N) Quantification of PLIN2$^+$IBA1$^+$cells per mm^2 of lesion at 14 dpi.
(O) Images of the lesioned corpus callosum of Cre− and Cre+ mice at 14 dpi demonstrating *Abca1* (green) and *Abcg1* (yellow) particles accumulating within IBA1$^+$ cells (magenta) visualized by RNA *in situ* hybridization. Scale bars, 20 μm.
(P) Quantification of *Abca1* and *Abcg1* particles within IBA1$^+$cells per lesion area at 14 dpi.
All data are mean ± SD; $^*p < 0.05$, $^{**}p < 0.001$, $^{***}p < 0.0001$; ns, not significant; two-tailed Welch's t test (B, D, F, H, I, K, N, and P), *n* numbers are indicated in the figure, each dot represents one mouse.
See also Figure S5.

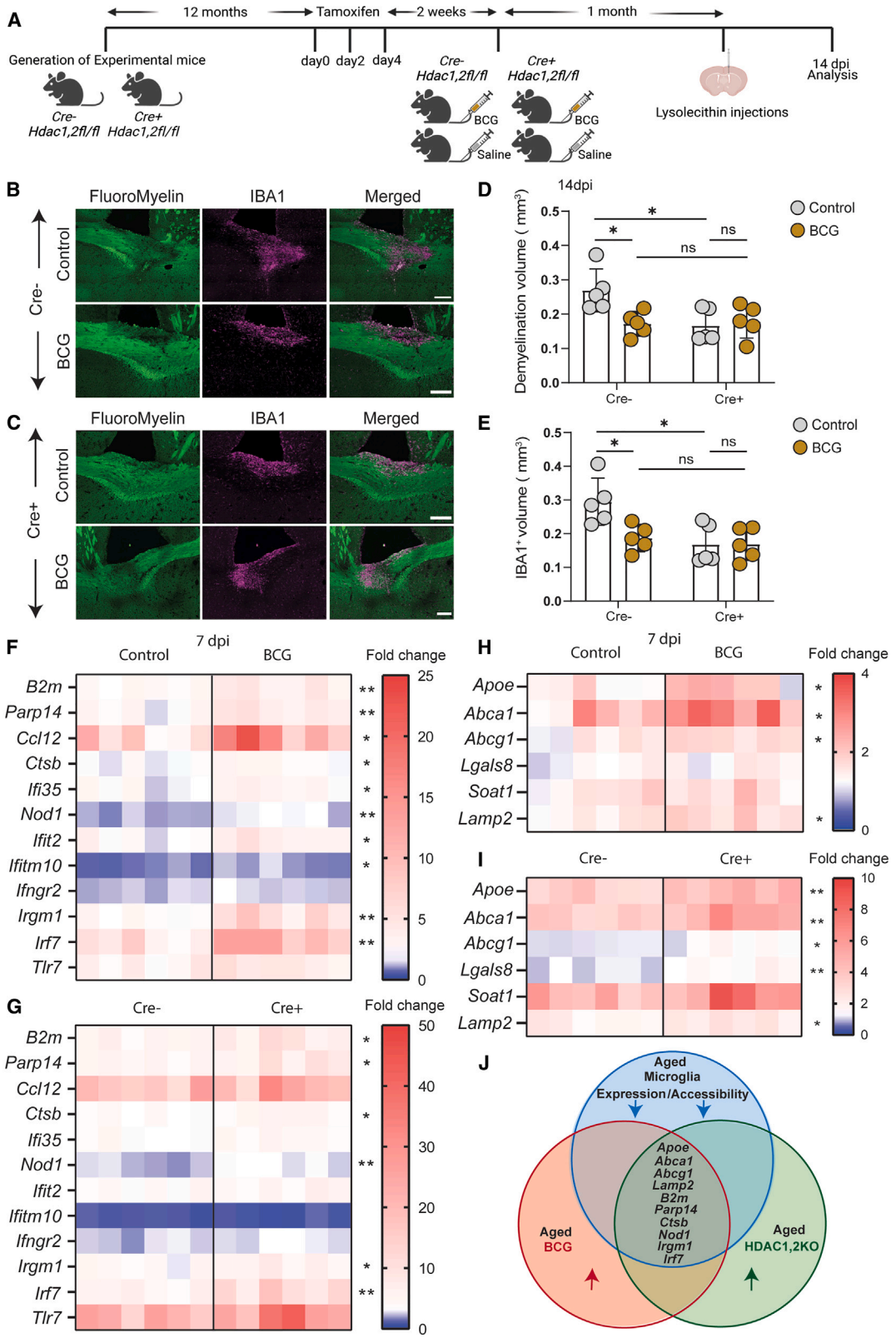

Figure 7. BCG-induced immune training is abolished in HDAC1/2 KO aged mice

(A) Schematic representation of BCG or saline treatment in *Cx3cr1*$^{creERT/het}$*Hdac1*$^{fl/fl}$*Hdac2*$^{fl/fl}$ and *Cx3cr1*$^{creERT/wt}$*Hdac1*$^{fl/fl}$*Hdac2*$^{fl/fl}$ aged mice

(B) Images of corpus callosum lesions in Cre− mice treated with BCG or saline at 14 dpi. Scale bars, 200 μm.

(legend continued on next page)

In response to BCG, we found that the core subunits involved in assembling the NuRD complex were differentially regulated in the brain. A recent study discovered a role for the transcription factor SPI1/PU.1 in regulating neuroinflammation by its association with a repressive complex containing HDAC1 in microglia.[58] Previous work has shown that HDAC1/2 function is time- and context-dependent in microglia.[47] Although prenatal depletion of HDAC1/2 leads to compromised proliferation and increased apoptosis induction, their role is dispensable for the homeostatic maintenance of adult microglia. Lack of HDAC1/2 in microglia in a mouse model of Alzheimer's disease induces genes involved in debris clearance, such as *Apoe*, *Axl*, and *Flt1*, and increases microglial phagocytosis of amyloid plaques.[47] In another study, in which HDAC1/2 was deleted in oligodendrocytes, a complete loss of mature oligodendrocytes with subsequent tremor and death during the first postnatal weeks, was observed.[59] Therapeutic approaches that are based on HDAC inhibition can, therefore, come with the side effect of interfering with oligodendrocyte differentiation and myelination. We used BCG as an approach to train immunity because of its preference for cells of the immune system, in particular those of the myeloid lineage. We found that BCG vaccination was able to enhance the pro-regenerative functions of microglia in aged mice, but not in those lacking HDAC1/2. Our data show that BCG vaccination leads to epigenetic and transcriptional changes of microglia, but how this occurs is unknown. One possibility is that peripheral immune cells or inflammatory cytokines released by cells in the periphery enter the brain. Our work is in line with a previous study showing that peripherally applied injections of low-dose lipopolysaccharides induce acute immune training of microglia in wild-type mice, but not in mice with a microglia-specific HDAC1/2 deletion,[27] suggesting that the acetylation status of histones is required for inducing memory. When priming microglia for innate immune functions in the aging brain, it is important to consider the diverse effects of age on microglia. As individuals age, the functionality of their immune system not only deteriorates, resulting in immunosenescence, but also undergoes a gain-of-function characterized by a pro-inflammatory state known as inflammaging.[18] Thus, the challenge for innate immune training protocols in aging will be to reprogram the innate immune system so that functions are re-gained without inducing maladaptive hyperinflammatory states. In the future, it will therefore be crucial to determine the precise molecular pathways that lead to long-term modulation of microglial responses. In sum, our data provide evidence that age-related epigenomic alterations contribute to poor pro-regenerative functions of microglia in aging, and we provide proof-of-principle that innate immune training of microglia can reverse such alterations and thereby increase pro-regenerative functions of microglia in demyelinating injury. These results align with the broader concept of an aberrant epigenetic state being a hallmark of aging,[60–63] and our findings offer evidence that such disturbances in the chromatin architecture create epigenetic rigidity that limits adaptive responses in cases of CNS injury.

Limitations of the study

In this study, we cannot rule out the possibility that other cell types, such as oligodendrocytes and non-myeloid cells, also respond to BCG treatment. Additionally, we did not investigate whether BCG's effects on myeloid cells are direct or indirect. Although our findings demonstrate that BCG vaccination induces epigenetic and transcriptional changes in microglia, the precise mechanisms remain unclear. One possibility is that peripheral immune cells or inflammatory cytokines released in response to BCG may enter the brain. Our data suggest that the effect of BCG could be partially explained by its impact on histone acetylation in microglia. However, not all regions affected by BCG vaccination are regulated by HDAC1/2 activity, indicating that many genes influenced by BCG are not under the control of HDAC1/2. Despite this, we propose that certain genes crucial for lesion recovery in demyelinating injuries are induced by BCG and regulated by HDAC1/2 activity.

STAR★METHODS

Detailed methods are provided in the online version of this paper and include the following:

- KEY RESOURCES TABLE
- RESOURCE AVAILABILITY
  - Lead contact
  - Materials availability
  - Data and code availability

(C) Images of corpus callosum lesions in Cre+ mice treated with BCG or saline at 14 dpi. Scale bars, 200 μm.
(D) Quantification of lesion volume in Cre− and Cre+ mice treated with BCG or saline at 14 dpi.
(E) Quantification of IBA1 volume in Cre− and Cre+ mice treated with BCG or saline at 14 dpi.
(F) Gene expression profile of a set of innate immune genes was determined using RT-qPCR in corpus callosum lesions at 7 dpi between control and BCG-treated aged mice.
(G) Gene expression profile of a set of innate immune genes was determined using RT-qPCR in corpus callosum lesions at 7 dpi between Cre− and Cre+ aged mice.
(H) Gene expression profile of a set of lipid metabolism genes was determined using RT-qPCR in corpus callosum lesions at 7 dpi between control and BCG-treated aged mice.
(I) Gene expression profile of a set of lipid metabolism genes was determined using RT-qPCR in corpus callosum lesions at 7 dpi between Cre− and Cre+ aged mice.
(J) Venn diagram indicating common sets of genes that are downregulated in aged microglia due to reduced accessibility but upregulated in HDAC1/2 KO and BCG-treated aged mice.
All data are mean ± SD; $*p < 0.05$, $**p < 0.001$, $***p < 0.0001$; ns, not significant; two-way *ANOVA* with Tukey's post hoc multiple comparison test (D and E) and two-tailed Student's t test (F–I), *n* numbers are indicated in the figure, each dot represents one mouse. Fold change of lesions in each group of gene expression profiles is normalized to no-lesion control and selected genes are in (Figures 3E, S3A–S3S, S4F, and S4G). Each square represents 1 lesion ($n = 6$ lesions/condition isolated from $n = 3$ biological replicates).
See also Table S4.

SUPPLEMENTAL INFORMATION

Supplemental information can be found online at https://doi.org/10.1016/j.immuni.2024.07.001.

ACKNOWLEDGMENTS

The work was supported by grants from the German Research Foundation (TRR 128-2, project ID 408885537-TRR 274, SyNergy Excellence Cluster, EXC2145, project ID390857198, GO 2694/4-1, PR 577/26-1, SI 746/15-1, and ImmunoSensation-EXC2151–390873048), the Human Frontier Science Program (HFSP), the ERC-ADG (101019594), and the Dr. Miriam and Sheldon G. Adelson Medical Research Foundation, Chan-Zuckerberg Initiative grant. NGS data production and data analysis were carried out at the DRESDEN-concept Genome Center, supported by the DFG Research Infrastructure Program (project 407482635) and part of the Next Generation Sequencing Competence Network NGS-CN (project 423957469).

AUTHOR CONTRIBUTIONS

M.S. and V.T. conceived the project and designed experiments. M.S. supervised the project. V.T., Y.A., A.D., H.J., L.L., N.N., G.G., K.B.L., and Q.W. carried out experiments or analyses. V.T. and B.P. analyzed and visualized sequencing datasets. J.M. and Z.S. helped in data acquisition. R.K., V.S., M.P., O.G., M.D., D.H.G., and M.S. provided essential tools or supervised data acquisition and analysis. V.T. visualized the data. M.S. and V.T. wrote the manuscript with input from all authors.

DECLARATION OF INTERESTS

The authors declare no competing interests.

Received: April 26, 2023
Revised: November 21, 2023
Accepted: July 1, 2024
Published: July 24, 2024

REFERENCES

1. Franklin, R.J.M., and Ffrench-Constant, C. (2017). Regenerating CNS myelin - from mechanisms to experimental medicines. Nat. Rev. Neurosci. *18*, 753–769. https://doi.org/10.1038/nrn.2017.136.
2. Plemel, J.R., Liu, W.Q., and Yong, V.W. (2017). Remyelination therapies: a new direction and challenge in multiple sclerosis. Nat. Rev. Drug Discov. *16*, 617–634. https://doi.org/10.1038/nrd.2017.115.
3. Lloyd, A.F., and Miron, V.E. (2019). The pro-remyelination properties of microglia in the central nervous system. Nat. Rev. Neurol. *15*, 447–458. https://doi.org/10.1038/s41582-019-0184-2.
4. Stadelmann, C., Timmler, S., Barrantes-Freer, A., and Simons, M. (2019). Myelin in the Central Nervous System: Structure, Function, and Pathology. Physiol. Rev. *99*, 1381–1431. https://doi.org/10.1152/physrev.00031.2018.
5. Franklin, R.J.M., and Simons, M. (2022). CNS remyelination and inflammation: From basic mechanisms to therapeutic opportunities. Neuron *110*, 3549–3565. https://doi.org/10.1016/j.neuron.2022.09.023.
6. Sim, F.J., Zhao, C., Penderis, J., and Franklin, R.J.M. (2002). The age-related decrease in CNS remyelination efficiency is attributable to an impairment of both oligodendrocyte progenitor recruitment and differentiation. J. Neurosci. *22*, 2451–2459.
7. Kotter, M.R., Li, W.W., Zhao, C., and Franklin, R.J.M. (2006). Myelin impairs CNS remyelination by inhibiting oligodendrocyte precursor cell differentiation. J. Neurosci. *26*, 328–332. https://doi.org/10.1523/JNEUROSCI.2615-05.2006.
8. Shen, S., Sandoval, J., Swiss, V.A., Li, J., Dupree, J., Franklin, R.J.M., and Casaccia-Bonnefil, P. (2008). Age-dependent epigenetic control of differentiation inhibitors is critical for remyelination efficiency. Nat. Neurosci. *11*, 1024–1034. https://doi.org/10.1038/nn.2172.
9. Ruckh, J.M., Zhao, J.W., Shadrach, J.L., van Wijngaarden, P., Rao, T.N., Wagers, A.J., and Franklin, R.J.M. (2012). Rejuvenation of regeneration in the aging central nervous system. Cell Stem Cell *10*, 96–103. https://doi.org/10.1016/j.stem.2011.11.019.
10. Cantuti-Castelvetri, L., Fitzner, D., Bosch-Queralt, M., Weil, M.T., Su, M., Sen, P., Ruhwedel, T., Mitkovski, M., Trendelenburg, G., Lütjohann, D., et al. (2018). Defective cholesterol clearance limits remyelination in the aged central nervous system. Science *359*, 684–688. https://doi.org/10.1126/science.aan4183.
11. Neumann, B., Baror, R., Zhao, C., Segel, M., Dietmann, S., Rawji, K.S., Foerster, S., McClain, C.R., Chalut, K., van Wijngaarden, P., and Franklin, R.J.M. (2019). Metformin Restores CNS Remyelination Capacity by Rejuvenating Aged Stem Cells. Cell Stem Cell *25*, 473–485.e8. https://doi.org/10.1016/j.stem.2019.08.015.
12. Bogie, J.F.J., Stinissen, P., and Hendriks, J.J.A. (2014). Macrophage subsets and microglia in multiple sclerosis. Acta Neuropathol. *128*, 191–213. https://doi.org/10.1007/s00401-014-1310-2.
13. Bogie, J.F.J., Grajchen, E., Wouters, E., Corrales, A.G., Dierckx, T., Vanherle, S., Mailleux, J., Gervois, P., Wolfs, E., Dehairs, J., et al. (2020). Stearoyl-CoA desaturase-1 impairs the reparative properties of macrophages and microglia in the brain. J. Exp. Med. *217*, e20191660. https://doi.org/10.1084/jem.20191660.
14. Bosch-Queralt, M., Cantuti-Castelvetri, L., Damkou, A., Schifferer, M., Schlepckow, K., Alexopoulos, I., Lütjohann, D., Klose, C., Vaculčiaková, L., Masuda, T., et al. (2021). Diet-dependent regulation of TGFβ impairs reparative innate immune responses after demyelination. Nat. Metab. *3*, 211–227. https://doi.org/10.1038/s42255-021-00341-7.
15. Berghoff, S.A., Spieth, L., Sun, T., Hosang, L., Schlaphoff, L., Depp, C., Düking, T., Winchenbach, J., Neuber, J., Ewers, D., et al. (2021). Microglia facilitate repair of demyelinated lesions via post-squalene sterol synthesis. Nat. Neurosci. *24*, 47–60. https://doi.org/10.1038/s41593-020-00757-6.
16. Evans, R.M., and Mangelsdorf, D.J. (2014). Nuclear Receptors, RXR, and the Big Bang. Cell *157*, 255–266. https://doi.org/10.1016/j.cell.2014.03.012.
17. Huang, J.K., Jarjour, A.A., Nait Oumesmar, B., Kerninon, C., Williams, A., Krezel, W., Kagechika, H., Bauer, J., Zhao, C., Baron-Van Evercooren, A., et al. (2011). Retinoid X receptor gamma signaling accelerates CNS remyelination. Nat. Neurosci. *14*, 45–53. https://doi.org/10.1038/nn.2702.
18. Franceschi, C., Garagnani, P., Parini, P., Giuliani, C., and Santoro, A. (2018). Inflammaging: a new immune–metabolic viewpoint for age-related diseases. Nat. Rev. Endocrinol. *14*, 576–590.

19. Safaiyan, S., Besson-Girard, S., Kaya, T., Cantuti-Castelvetri, L., Liu, L., Ji, H., Schifferer, M., Gouna, G., Usifo, F., Kannaiyan, N., et al. (2021). White matter aging drives microglial diversity. Neuron *109*, 1100–1117.e10. https://doi.org/10.1016/j.neuron.2021.01.027.

20. Allis, C.D., and Jenuwein, T. (2016). The molecular hallmarks of epigenetic control. Nat. Rev. Genet. *17*, 487–500. https://doi.org/10.1038/nrg.2016.59.

21. Netea, M.G., Quintin, J., and van der Meer, J.W.M. (2011). Trained immunity: a memory for innate host defense. Cell Host Microbe *9*, 355–361. https://doi.org/10.1016/j.chom.2011.04.006.

22. Netea, M.G., Latz, E., Mills, K.H.G., and O'Neill, L.A.J. (2015). Innate immune memory: a paradigm shift in understanding host defense. Nat. Immunol. *16*, 675–679. https://doi.org/10.1038/ni.3178.

23. Netea, M.G., Joosten, L.A.B., Latz, E., Mills, K.H.G., Natoli, G., Stunnenberg, H.G., O'Neill, L.A.J., and Xavier, R.J. (2016). Trained immunity: A program of innate immune memory in health and disease. Science *352*, aaf1098. https://doi.org/10.1126/science.aaf1098.

24. Neher, J.J., and Cunningham, C. (2019). Priming Microglia for Innate Immune Memory in the Brain. Trends Immunol. *40*, 358–374. https://doi.org/10.1016/j.it.2019.02.001.

25. Fanucchi, S., Domínguez-Andrés, J., Joosten, L.A.B., Netea, M.G., and Mhlanga, M.M. (2021). The Intersection of Epigenetics and Metabolism in Trained Immunity. Immunity *54*, 32–43. https://doi.org/10.1016/j.immuni.2020.10.011.

26. Füger, P., Hefendehl, J.K., Veeraraghavalu, K., Wendeln, A.C., Schlosser, C., Obermüller, U., Wegenast-Braun, B.M., Neher, J.J., Martus, P., Kohsaka, S., et al. (2017). Microglia turnover with aging and in an Alzheimer's model via long-term in vivo single-cell imaging. Nat. Neurosci. *20*, 1371–1376. https://doi.org/10.1038/nn.4631.

27. Wendeln, A.C., Degenhardt, K., Kaurani, L., Gertig, M., Ulas, T., Jain, G., Wagner, J., Häsler, L.M., Wild, K., Skodras, A., et al. (2018). Innate immune memory in the brain shapes neurological disease hallmarks. Nature *556*, 332–338. https://doi.org/10.1038/s41586-018-0023-4.

28. Kaufmann, E., Sanz, J., Dunn, J.L., Khan, N., Mendonca, L.E., Pacis, A., Tzelepis, F., Pernet, E., Dumaine, A., Grenier, J.C., et al. (2018). BCG Educates Hematopoietic Stem Cells to Generate Protective Innate Immunity against Tuberculosis. Cell *172*, 176–190.e19. https://doi.org/10.1016/j.cell.2017.12.031.

29. Garly, M.L., Martins, C.L., Balé, C., Baldé, M.A., Hedegaard, K.L., Gustafson, P., Lisse, I.M., Whittle, H.C., and Aaby, P. (2003). BCG scar and positive tuberculin reaction associated with reduced child mortality in West Africa. A non-specific beneficial effect of BCG? Vaccine *21*, 2782–2790. https://doi.org/10.1016/s0264-410x(03)00181-6.

30. Lampron, A., Larochelle, A., Laflamme, N., Préfontaine, P., Plante, M.M., Sánchez, M.G., Yong, V.W., Stys, P.K., Tremblay, M.È., and Rivest, S. (2015). Inefficient clearance of myelin debris by microglia impairs remyelinating processes. J. Exp. Med. *212*, 481–495. https://doi.org/10.1084/jem.20141656.

31. Cunha, M.I., Su, M., Cantuti-Castelvetri, L., Müller, S.A., Schifferer, M., Djannatian, M., Alexopoulos, I., van der Meer, F., Winkler, A., van Ham, T.J., et al. (2020). Pro-inflammatory activation following demyelination is required for myelin clearance and oligodendrogenesis. J. Exp. Med. *217*, e20191390. https://doi.org/10.1084/jem.20191390.

32. Miron, V.E., Boyd, A., Zhao, J.W., Yuen, T.J., Ruckh, J.M., Shadrach, J.L., van Wijngaarden, P., Wagers, A.J., Williams, A., Franklin, R.J.M., and ffrench-Constant, C. (2013). M2 microglia and macrophages drive oligodendrocyte differentiation during CNS remyelination. Nat. Neurosci. *16*, 1211–1218. https://doi.org/10.1038/nn.3469.

33. Lloyd, A.F., Davies, C.L., Holloway, R.K., Labrak, Y., Ireland, G., Carradori, D., Dillenburg, A., Borger, E., Soong, D., Richardson, J.C., et al. (2019). Central nervous system regeneration is driven by microglia necroptosis and repopulation. Nat. Neurosci. *22*, 1046–1052. https://doi.org/10.1038/s41593-019-0418-z.

34. Plemel, J.R., Stratton, J.A., Michaels, N.J., Rawji, K.S., Zhang, E., Sinha, S., Baaklini, C.S., Dong, Y., Ho, M., Thorburn, K., et al. (2020). Microglia response following acute demyelination is heterogeneous and limits infiltrating macrophage dispersion. Sci. Adv. *6*, eaay6324. https://doi.org/10.1126/sciadv.aay6324.

35. Jeffery, N.D., and Blakemore, W.F. (1995). Remyelination of mouse spinal cord axons demyelinated by local injection of lysolecithin. J. Neurocytol. *24*, 775–781.

36. Masuda, T., Sankowski, R., Staszewski, O., Böttcher, C., Amann, L., Sagar, S., Scheiwe, C., Nessler, S., Kunz, P., van Loo, G., et al. (2019). Spatial and temporal heterogeneity of mouse and human microglia at single-cell resolution. Nature *566*, 388–392. https://doi.org/10.1038/s41586-019-0924-x.

37. Krasemann, S., Madore, C., Cialic, R., Baufeld, C., Calcagno, N., El Fatimy, R., Beckers, L., O'Loughlin, E., Xu, Y., Fanek, Z., et al. (2017). The TREM2-APOE Pathway Drives the Transcriptional Phenotype of Dysfunctional Microglia in Neurodegenerative Diseases. Immunity *47*, 566–581.e9. https://doi.org/10.1016/j.immuni.2017.08.008.

38. Hammond, T.R., Dufort, C., Dissing-Olesen, L., Giera, S., Young, A., Wysoker, A., Walker, A.J., Gergits, F., Segel, M., Nemesh, J., et al. (2019). Single-Cell RNA Sequencing of Microglia throughout the Mouse Lifespan and in the Injured Brain Reveals Complex Cell-State Changes. Immunity *50*, 253–271.e6. https://doi.org/10.1016/j.immuni.2018.11.004.

39. Sala Frigerio, C., Wolfs, L., Fattorelli, N., Thrupp, N., Voytyuk, I., Schmidt, I., Mancuso, R., Chen, W.T., Woodbury, M.E., Srivastava, G., et al. (2019). The Major Risk Factors for Alzheimer's Disease: Age, Sex, and Genes Modulate the Microglia Response to Abeta Plaques. Cell Rep. *27*, 1293–1306.e6. https://doi.org/10.1016/j.celrep.2019.03.099.

40. Keren-Shaul, H., Spinrad, A., Weiner, A., Matcovitch-Natan, O., Dvir-Szternfeld, R., Ulland, T.K., David, E., Baruch, K., Lara-Astaiso, D., Toth, B., et al. (2017). A Unique Microglia Type Associated with Restricting Development of Alzheimer's Disease. Cell *169*, 1276–1290.e17. https://doi.org/10.1016/j.cell.2017.05.018.

41. Li, X., Egervari, G., Wang, Y., Berger, S.L., and Lu, Z. (2018). Regulation of chromatin and gene expression by metabolic enzymes and metabolites. Nat. Rev. Mol. Cell Biol. *19*, 563–578. https://doi.org/10.1038/s41580-018-0029-7.

42. Dai, Z., Ramesh, V., and Locasale, J.W. (2020). The evolving metabolic landscape of chromatin biology and epigenetics. Nat. Rev. Genet. *21*, 737–753. https://doi.org/10.1038/s41576-020-0270-8.

43. Kleinnijenhuis, J., Quintin, J., Preijers, F., Joosten, L.A.B., Ifrim, D.C., Saeed, S., Jacobs, C., van Loenhout, J., de Jong, D., Stunnenberg, H.G., et al. (2012). Bacille Calmette-Guerin induces NOD2-dependent nonspecific protection from reinfection via epigenetic reprogramming of monocytes. Proc. Natl. Acad. Sci. USA *109*, 17537–17542. https://doi.org/10.1073/pnas.1202870109.

44. Arts, R.J.W., Carvalho, A., La Rocca, C., Palma, C., Rodrigues, F., Silvestre, R., Kleinnijenhuis, J., Lachmandas, E., Gonçalves, L.G., Belinha, A., et al. (2016). Immunometabolic Pathways in BCG-Induced Trained Immunity. Cell Rep. *17*, 2562–2571. https://doi.org/10.1016/j.celrep.2016.11.011.

45. Fielding, C.J., and Fielding, P.E. (1995). Molecular physiology of reverse cholesterol transport. J. Lipid Res. *36*, 211–228.

46. Seto, E., and Yoshida, M. (2014). Erasers of histone acetylation: the histone deacetylase enzymes. Cold Spring Harb. Perspect. Biol. *6*, a018713. https://doi.org/10.1101/cshperspect.a018713.

47. Datta, M., Staszewski, O., Raschi, E., Frosch, M., Hagemeyer, N., Tay, T.L., Blank, T., Kreutzfeldt, M., Merkler, D., Ziegler-Waldkirch, S., et al. (2018). Histone Deacetylases 1 and 2 Regulate Microglia Function during Development, Homeostasis, and Neurodegeneration in a Context-Dependent Manner. Immunity *48*, 514–529.e6. https://doi.org/10.1016/j.immuni.2018.02.016.

48. Goldmann, T., Wieghofer, P., Müller, P.F., Wolf, Y., Varol, D., Yona, S., Brendecke, S.M., Kierdorf, K., Staszewski, O., Datta, M., et al. (2013). A new type of microglia gene targeting shows TAK1 to be pivotal in CNS autoimmune inflammation. Nat. Neurosci. *16*, 1618–1626. https://doi.org/10.1038/nn.3531.

49. Perry, V.H., and Holmes, C. (2014). Microglial priming in neurodegenerative disease. Nat. Rev. Neurol. *10*, 217–224. https://doi.org/10.1038/nrneurol.2014.38.

50. Perry, V.H., Cunningham, C., and Holmes, C. (2007). Systemic infections and inflammation affect chronic neurodegeneration. Nat. Rev. Immunol. *7*, 161–167. https://doi.org/10.1038/nri2015.

51. Cunningham, C., Wilcockson, D.C., Campion, S., Lunnon, K., and Perry, V.H. (2005). Central and systemic endotoxin challenges exacerbate the local inflammatory response and increase neuronal death during chronic neurodegeneration. J. Neurosci. *25*, 9275–9284. https://doi.org/10.1523/JNEUROSCI.2614-05.2005.

52. Gómez-Nicola, D., Schetters, S.T.T., and Perry, V.H. (2014). Differential role of CCR2 in the dynamics of microglia and perivascular macrophages during prion disease. Glia *62*, 1041–1052. https://doi.org/10.1002/glia.22660.

53. Zhang, X., Kracht, L., Lerario, A.M., Dubbelaar, M.L., Brouwer, N., Wesseling, E.M., Boddeke, E.W.G.M., Eggen, B.J.L., and Kooistra, S.M. (2022). Epigenetic regulation of innate immune memory in microglia. J. Neuroinflammation *19*, 111. https://doi.org/10.1186/s12974-022-02463-5.

54. Hickman, S.E., Kingery, N.D., Ohsumi, T.K., Borowsky, M.L., Wang, L.C., Means, T.K., and El Khoury, J. (2013). The microglial sensome revealed by direct RNA sequencing. Nat. Neurosci. *16*, 1896–1905. https://doi.org/10.1038/nn.3554.

55. Prinz, M., and Priller, J. (2014). Microglia and brain macrophages in the molecular age: from origin to neuropsychiatric disease. Nat. Rev. Neurosci. *15*, 300–312. https://doi.org/10.1038/nrn3722.

56. Heneka, M.T., Kummer, M.P., and Latz, E. (2014). Innate immune activation in neurodegenerative disease. Nat. Rev. Immunol. *14*, 463–477. https://doi.org/10.1038/nri3705.

57. Deczkowska, A., Keren-Shaul, H., Weiner, A., Colonna, M., Schwartz, M., and Amit, I. (2018). Disease-Associated Microglia: A Universal Immune Sensor of Neurodegeneration. Cell *173*, 1073–1081. https://doi.org/10.1016/j.cell.2018.05.003.

58. Ralvenius, W.T., Mungenast, A.E., Woolf, H., Huston, M.M., Gillingham, T.Z., Godin, S.K., Penney, J., Cam, H.P., Gao, F., Fernandez, C.G., et al. (2023). A novel molecular class that recruits HDAC/MECP2 complexes to PU.1 motifs reduces neuroinflammation. J. Exp. Med. *220*, e20222105. https://doi.org/10.1084/jem.20222105.

59. Ye, F., Chen, Y., Hoang, T., Montgomery, R.L., Zhao, X.H., Bu, H., Hu, T., Taketo, M.M., van Es, J.H., Clevers, H., et al. (2009). HDAC1 and HDAC2 regulate oligodendrocyte differentiation by disrupting the beta-catenin-TCF interaction. Nat. Neurosci. *12*, 829–838. https://doi.org/10.1038/nn.2333.

60. Calvanese, V., Lara, E., Kahn, A., and Fraga, M.F. (2009). The role of epigenetics in aging and age-related diseases. Ageing Res. Rev. *8*, 268–276. https://doi.org/10.1016/j.arr.2009.03.004.

61. Copray, S., Huynh, J.L., Sher, F., Casaccia-Bonnefil, P., and Boddeke, E. (2009). Epigenetic mechanisms facilitating oligodendrocyte development, maturation, and aging. Glia *57*, 1579–1587. https://doi.org/10.1002/glia.20881.

62. López-Otín, C., Blasco, M.A., Partridge, L., Serrano, M., and Kroemer, G. (2013). The hallmarks of aging. Cell *153*, 1194–1217. https://doi.org/10.1016/j.cell.2013.05.039.

63. Pal, S., and Tyler, J.K. (2016). Epigenetics and aging. Sci. Adv. *2*, e1600584. https://doi.org/10.1126/sciadv.1600584.

64. Welch, J.D., Kozareva, V., Ferreira, A., Vanderburg, C., Martin, C., and Macosko, E.Z. (2019). Single-Cell Multi-omic Integration Compares and Contrasts Features of Brain Cell Identity. Cell *177*, 1873–1887.e17. https://doi.org/10.1016/j.cell.2019.05.006.

65. McGinnis, C.S., Murrow, L.M., and Gartner, Z.J. (2019). DoubletFinder: Doublet Detection in Single-Cell RNA Sequencing Data Using Artificial Nearest Neighbors. Cell Syst. *8*, 329–337.e4. https://doi.org/10.1016/j.cels.2019.03.003.

66. Satija, R., Farrell, J.A., Gennert, D., Schier, A.F., and Regev, A. (2015). Spatial reconstruction of single-cell gene expression data. Nat. Biotechnol. *33*, 495–502. https://doi.org/10.1038/nbt.3192.

67. Robinson, J.T., Thorvaldsdóttir, H., Winckler, W., Guttman, M., Lander, E.S., Getz, G., and Mesirov, J.P. (2011). Integrative genomics viewer. Nat. Biotechnol. *29*, 24–26. https://doi.org/10.1038/nbt.1754.

68. Martin, M. (2011). Cutadapt removes adapter sequences from high-throughput sequencing reads. EMBnet.journal. *17*, 10–12. https://doi.org/10.14806/ej.17.1.200.

69. Langmead, B., and Salzberg, S.L. (2012). Fast gapped-read alignment with Bowtie 2. Nat. Methods *9*, 357–359. https://doi.org/10.1038/nmeth.1923.

70. Barnett, D.W., Garrison, E.K., Quinlan, A.R., Strömberg, M.P., and Marth, G.T. (2011). BamTools: a C++ API and toolkit for analyzing and managing BAM files. Bioinformatics *27*, 1691–1692. https://doi.org/10.1093/bioinformatics/btr174.

71. Ramírez, F., Dündar, F., Diehl, S., Grüning, B.A., and Manke, T. (2014). deepTools: a flexible platform for exploring deep-sequencing data. Nucleic Acids Res. *42*, W187–W191. https://doi.org/10.1093/nar/gku365.

72. Zhang, Y., Liu, T., Meyer, C.A., Eeckhoute, J., Johnson, D.S., Bernstein, B.E., Nusbaum, C., Myers, R.M., Brown, M., Li, W., and Liu, X.S. (2008). Model-based analysis of ChIP-Seq (MACS). Genome Biol. *9*, R137. https://doi.org/10.1186/gb-2008-9-9-r137.

73. Lun, A.T.L., and Smyth, G.K. (2016). csaw: a Bioconductor package for differential binding analysis of ChIP-seq data using sliding windows. Nucleic Acids Res. *44*, e45. https://doi.org/10.1093/nar/gkv1191.

74. Heinz, S., Benner, C., Spann, N., Bertolino, E., Lin, Y.C., Laslo, P., Cheng, J.X., Murre, C., Singh, H., and Glass, C.K. (2010). Simple combinations of lineage-determining transcription factors prime cis-regulatory elements required for macrophage and B cell identities. Mol. Cell *38*, 576–589. https://doi.org/10.1016/j.molcel.2010.05.004.

75. Dobin, A., Davis, C.A., Schlesinger, F., Drenkow, J., Zaleski, C., Jha, S., Batut, P., and Chaisson, M. (2013). Gingeras TR. STAR: ultrafast universal RNA-seq aligner. Bioinformatics *29*, 15–21. https://doi.org/10.1093/bioinformatics/bts635.

76. Liao, Y., Smyth, G.K., and Shi, W. (2014). featureCounts: an efficient general purpose program for assigning sequence reads to genomic features. Bioinformatics *30*, 923–930. https://doi.org/10.1093/bioinformatics/btt656.

77. Love, M.I., Huber, W., and Anders, S. (2014). Moderated estimation of fold change and dispersion for RNA-seq data with DESeq2. Genome Biol. *15*, 550. https://doi.org/10.1186/s13059-014-0550-8.

78. Büttner, M., Ostner, J., Müller, C.L., Theis, F.J., and Schubert, B. (2021). scCODA is a Bayesian model for compositional single-cell data analysis. Nat. Commun. *12*, 6876. https://doi.org/10.1038/s41467-021-27150-6.

79. Supek, F., Bošnjak, M., Škunca, N., and Šmuc, T. (2011). REVIGO summarizes and visualizes long lists of gene ontology terms. PLoS One *6*, e21800. https://doi.org/10.1371/journal.pone.0021800.

80. Schindelin, J., Arganda-Carreras, I., Frise, E., Kaynig, V., Longair, M., Pietzsch, T., Preibisch, S., Rueden, C., Saalfeld, S., Schmid, B., et al. (2012). Fiji: an open-source platform for biological-image analysis. Nat. Methods *9*, 676–682. https://doi.org/10.1038/nmeth.2019.

81. Bosch-Queralt, M., Tiwari, V., Damkou, A., Vaculčiaková, L., Alexopoulos, I., and Simons, M. (2022). A fluorescence microscopy-based protocol for volumetric measurement of lysolecithin lesion-associated de- and re-myelination in mouse brain. Star Protoc. *3*, 101141. https://doi.org/10.1016/j.xpro.2022.101141.

82. Duewell, P., Kono, H., Rayner, K.J., Sirois, C.M., Vladimer, G., Bauernfeind, F.G., Abela, G.S., Franchi, L., Nuñez, G., Schnurr, M., et al. (2010). NLRP3 inflammasomes are required for atherogenesis and activated by cholesterol crystals. Nature *464*, 1357–1361. https://doi.org/10.1038/nature08938.

83. Liu, L., Besson-Girard, S., Ji, H., Gehring, K., Bulut, B., Kaya, T., Usifo, F., Simons, M., and Gokce, O. (2021). Dissociation of microdissected mouse

brain tissue for artifact free single-cell RNA sequencing. STAR Protoc. *2*, 100590. https://doi.org/10.1016/j.xpro.2021.100590.

84. Corces, M.R., Trevino, A.E., Hamilton, E.G., Greenside, P.G., Sinnott-Armstrong, N.A., Vesuna, S., Satpathy, A.T., Rubin, A.J., Montine, K.S., Wu, B., et al. (2017). An improved ATAC-seq protocol reduces background and enables interrogation of frozen tissues. Nat. Methods *14*, 959–962. https://doi.org/10.1038/nmeth.4396.

85. Rosenberg, A.B., Roco, C.M., Muscat, R.A., Kuchina, A., Sample, P., Yao, Z., Graybuck, L.T., Peeler, D.J., Mukherjee, S., Chen, W., et al. (2018). Single-cell profiling of the developing mouse brain and spinal cord with split-pool barcoding. Science *360*, 176–182. https://doi.org/10.1126/science.aam8999.

86. Buenrostro, J.D., Giresi, P.G., Zaba, L.C., Chang, H.Y., and Greenleaf, W.J. (2013). Transposition of native chromatin for fast and sensitive epigenomic profiling of open chromatin, DNA-binding proteins and nucleosome position. Nat. Methods *10*, 1213–1218. https://doi.org/10.1038/nmeth.2688.

87. Fujiwara, S., Baek, S., Varticovski, L., Kim, S., and Hager, G.L. (2019). High Quality ATAC-Seq Data Recovered from Cryopreserved Breast Cell Lines and Tissue. Sci. Rep. *9*, 516. https://doi.org/10.1038/s41598-018-36927-7.

88. Ji, H., Besson-Girard, S., Androvic, P., Bulut, B., Liu, L., Wang, Y., and Gokce, O. (2023). High-Resolution RNA Sequencing from PFA-Fixed Microscopy Sections. Methods Mol. Biol. *2616*, 205–212. https://doi.org/10.1007/978-1-0716-2926-0_16.

89. Kaya, T., Mattugini, N., Liu, L., Ji, H., Cantuti-Castelvetri, L., Wu, J., Schifferer, M., Groh, J., Martini, R., Besson-Girard, S., et al. (2022). CD8(+) T cells induce interferon-responsive oligodendrocytes and microglia in white matter aging. Nat. Neurosci. *25*, 1446–1457. https://doi.org/10.1038/s41593-022-01183-6.

90. Novakovic, B., Habibi, E., Wang, S.Y., Arts, R.J.W., Davar, R., Megchelenbrink, W., Kim, B., Kuznetsova, T., Kox, M., Zwaag, J., et al. (2016). β-Glucan Reverses the Epigenetic State of LPS-Induced Immunological Tolerance. Cell *167*, 1354–1368.e14. https://doi.org/10.1016/j.cell.2016.09.034.

91. Blake, J.A., and Harris, M.A. (2008). The Gene Ontology (GO) project: structured vocabularies for molecular biology and their application to genome and expression analysis. Curr Protoc Bioinformatics *Chapter 7*, 7.2.1–7.2.9. https://doi.org/10.1002/0471250953.bi0702s23.

92. Timmons, J.A., Szkop, K.J., and Gallagher, I.J. (2015). Multiple sources of bias confound functional enrichment analysis of global -omics data. Genome Biol. *16*, 186. https://doi.org/10.1186/s13059-015-0761-7.

STAR★METHODS

KEY RESOURCES TABLE

REAGENT or RESOURCE	SOURCE	IDENTIFIER
Antibodies		
Rabbit anti-IBA1	Wako	Cat# 019-19741; RRID:AB_839504
Chicken anti-IBA1	Synaptic systems	Cat# 234 009; RRID:AB_2891282
Guinea pig anti-IBA1	Synaptic systems	Cat# 234 308; RRID:AB_2924932
Rat anti-MAC2	Bio legend	Cat# 125402; RRID:AB_1134238
Rat anti-MHCII	Thermofisher Scientific	Cat# 14-5321-81; RRID:AB_467560
Rabbit anti-PLIN2	Novus Biologicals	Cat#NB11040877; RRID:AB_787904
Rabbit anti-OLIG2	Millipore	Cat# AB9610; RRID:AB_570666
Rabbit anti-BCAS1	Synaptic systems (Custom made)	https://www.science.org/doi/10.1126/scitranslmed.aam7816
Mouse anti-APC-CC1	Millipore	Cat# OP80; RRID:AB_2057371
Rat anti-LAMP1	Santa Cruz Biotechnology	Cat# sc-19992; RRID:AB_2134495
AffiniPure Fab fragment	Jackson ImmunoResearch	Cat# 715-007-003; RRID:AB_2307338
Rat anti-CD45	Thermofisher Scientific	Cat#48-0451-82; RRID:AB_1518806
Rat anti-CD11b	Bio legend	Cat#101228; RRID:AB_893232
Rat anti-Ly6C	Bio legend	Cat#128029; RRID:AB_10896061
Rat anti-Ly6G	Thermofisher Scientific	Cat#61-9668-82; RRID:AB_2574679
Rat anti-F4/80	Thermofisher Scientific	Cat#25-4801-82; RRID:AB_469653
Rat anti-CD16/CD32	Thermofisher Scientific	Cat# 14-0161-82; RRID:AB_467133
Rabbit anti- Histone (H3K4me3)	Diagenode	Cat# C15410003; RRID:AB_2924768
Rabbit anti- Histone (H3K27ac)	Diagenode	Cat# C15410196; RRID:AB_2637079
Rabbit negative Ctrl IgG	Diagenode	Cat#C15410206; RRID:AB_2722554
Alexa Fluor 555	Thermofisher Scientific	Cat# A-21422; RRID:AB_2535844
Alexa Fluor 555	Thermofisher Scientific	Cat# A-21428; RRID:AB_2535849
Alexa Fluor 647	Thermofisher Scientific	Cat# A-21244; RRID:AB_2535812
Alexa Fluor 647	Thermofisher Scientific	Cat# A-21450; RRID:AB_141882
Alexa Fluor 647	Jackson ImmunoResearch	Cat# 712605150; RRID:AB_2340693
Bacterial and virus strains		
BCG (Bacillus Calmette Guérin, RIVM strain)	Medac GmBH	N/A
Chemicals, peptides, and recombinant proteins		
FluoroMyelin	Thermofisher Scientific	Cat# F34651
DAPI	Thermofisher Scientific	Cat# D1306
Tamoxifen	Sigma-Aldrich	Cat# T5648
Zombie	Biolegend	Cat# 423105
L-α-lyso-Lecithin (Lysolecithin)	Sigma-Aldrich	Cat# L4129
Actinomycin-D	Sigma-Aldrich	Cat# A1410
Critical commercial assays		
Invisorb Spin Tissue Mini Kit	Invitek	Cat# 1032100300
Adult tissue dissociation kit	Miltenyi Biotech	Cat# 130-107-677
RNeasy Plus Mini kit	QIAGEN	Cat# 74134
Superscript III First strand Synthesis	Thermo fisher Scientific	Cat# 18080051
PowerUp SYBR Green Master Mix	Thermo fisher Scientific	Cat# A25742
RNAscope Multiplex Fluorescent v2 assay	Advanced cell Diagnostics	Cat# 323100
Chromium Next Gen Single Cell 3' HT kit v3.1	Illumina	Cat# 1000348
iDeal ChIP-seq kit for Histones	Diagenode	Cat# C01010059

(*Continued on next page*)

Continued

REAGENT or RESOURCE	SOURCE	IDENTIFIER
High Sensitivity NGS Fragment Analysis Kit	Agilent	Cat# DNF-474
DNA Clear & Concentrator TM-5 kit	Zymo-research	Cat# D4014
IP-Star® Compact Automated System	Diagenode	Cat# B03000002
MicroPlex Library Preparation Kit v3 /96 rxns	Diagenode	Cat# C05010002
Qubit™ dsDNA HS Assay Kit	Thermofisher Scientific	Cat# Q32854
HDAC1 Fluorogenic Assay Kit	BPS bioscience	Cat#50061
HDAC2 Fluorogenic Assay Kit	BPS bioscience	Cat#50062
Deposited data		
Raw and analyzed data	This paper	GEO (GSE230187, GSE230190, GSE230191, GSE230480, GSE247529)
Experimental models: Organisms/strains		
Mouse: C57BL/6JRj	JANVIER labs	RRID:IMSR_RJ:C57BL-6JRJ
Mouse: *Cx3cr1*^{creERT2}*x Hdac1,2*^{flox}	Datta et al.[47]	N/A
Oligonucleotides		
Primers	Table S4	N/A
Software and algorithms		
R	https://www.r-project.org/	RRID:SCR_001905
R studio	https://www.rstudio.com/	Version 4.2 and 4.3
LIGER	Welch et al.[64]	RRID:SCR_018100
Cell ranger	10x genomics	v(6.1.0); RRID:SCR_017344
Doublet finder	McGinnis et al.[65]	v(2.0.2); RRID:SCR_018771
scCustomise	https://doi.org/10.5281/zenodo.5706430	RRID:SCR_024675
Seurat	Satija et al.[66]	v(4.0.6; 4.4.0); RRID:SCR_016341
Galaxy	https://usegalaxy.eu/	RRID:SCR_006281
IGV	Robinson et al.[67]	RRID:SCR_011793
Trim galore	http://www.bioinformatics.babraham.ac.uk/projects/trim_galore/	RRID:SCR_011847
Cutadapt	Martin[68]	RRID:SCR_011841
Bowtie2	Langmead and Salzberg[69]	RRID:SCR_016368
BAM tools	Barnett et al.[70]	RRID:SCR_015987
Picard tools	http://broadinstitute.github.io/picard	RRID:SCR_006525
Deep tools	Ramírez et al.[71]	RRID:SCR_016366
MACS2	Zhang et al.[72]	RRID:SCR_013291
Csaw	Lun and Smyth[73]	https://doi.org/10.1093/nar/gkv1191
FindMotifsGenome tool	Heinz et al.[74]	http://homer.ucsd.edu/homer/motif/
STAR	Dobin et al.[75]	RRID:SCR_004463
Feature counts	Liao et al.[76]	RRID:SCR_012919
Deseq2	Love et al.[77]	RRID:SCR_015687
Gene ontology (GO) enrichment analysis	http://www.geneontology.org	RRID:SCR_002811
scCODA	Büttner et al.[78]	https://github.com/theislab/scCODA
Revigo	Supek et al.[79]	RRID:SCR_005825
Cytoscape	https://cytoscape.org/	RRID:SCR_003032
Graph Pad Prism	https://www.graphpad.com/	RRID:SCR_002798
Image Lab Software	Bio-Rad	RRID:SCR_014210
ImageJ (Fiji)	Schindelin et al.[80]	RRID:SCR_002285
Adobe Illustrator	https://www.adobe.com/	RRID:SCR_010279
Code for calculating the lesion volume	Bosch-Queralt et al.[81]	https://github.com/lenkavaculciakova/lesion_volume

(*Continued on next page*)

Continued

REAGENT or RESOURCE	SOURCE	IDENTIFIER
Other		
Nuclei EZ Prep lysis buffer	Millipore Sigma	Cat# NUC101
UltraPure SSPE, 20X	Thermofisher Scientific	Cat# 15591043
OptiPrep™ Density Gradient Medium	Millipore Sigma	Cat# D1556
PKD buffer	QIAGEN	Cat# 157014133
Tween-20	Bio-Rad	Cat# 1610781
RNase inhibitor	Takara-Bio	Cat# 2313A
Oligo dT25 magnetic beads	Invitrogen	Cat# 61005
Cell Lysis Buffer (10X)	Cell Signalling Technology	Cat# 9803
Proteinase K solution	QIAGEN	Cat# 19131
RNAscope Probe-Mm-Tnf-a,	Advanced cell Diagnostics	Cat# 311081
RNAscope Probe-Mm-Il1b-C2	Advanced cell Diagnostics	Cat# 316891-C2
RNAscope Probe-Mm-Abca1	Advanced cell Diagnostics	Cat# 522251
RNAscope Probe-Mm-Abcg1-C2	Advanced cell Diagnostics	Cat# 422221-C2
RNAscope Probe-Mm-Nr1h2	Advanced cell Diagnostics	Cat# 563261
RNAscope Probe-Mm-Irf7-C2	Advanced cell Diagnostics	Cat#534541-C2
RNAscope Probe-Mm-Irgm1-C2	Advanced cell Diagnostics	Cat#588931-C2
RNAscope Probe-Mm-Parp14-C1	Advanced cell Diagnostics	Cat#1093331-C1
RNAscope Probe-Mm-Lamp2-C2	Advanced cell Diagnostics	Cat#422851-C2
RNAscope 3-Plex Negative Control Probe_Mm	Advanced cell Diagnostics	Cat# 320871
RNAscope 3-plex Positive Control Probe_Mm	Advanced cell Diagnostics	Cat# 320881

RESOURCE AVAILABILITY

Lead contact

Further information and requests for resources and reagents should be directed to and will be fulfilled by the lead contact, Mikael Simons (mikael.simons@dzne.de).

Materials availability

Reagents generated in this study are available from the lead contact with a completed Material Transfer Agree.

Data and code availability

- The datasets we generated (snRNA-seq, ATAC seq, Chip Seq, Bulk RNA seq) have been deposited at GEO (NCBI) and are publically available from the date of publication. Accession numbers are listed in the key resources table. All other data that supports findings are available upon request from the lead contact.
- This paper does not report original code.
- Any additional information required to reanalyze the data reported in this paper is available from the lead contact upon request.

EXPERIMENTAL MODEL AND STUDY PARTICIPANT DETAILS

Mice

Mice were housed in the animal facility of the German Centre for Neurodegenerative Diseases (DZNE), Munich, in a standard, pathogen-free, 12-hour light-dark cycle and with ad libitum access to food and water. The animal facility maintained a temperature of 20 to 22°C and 40 to 60% humidity. All C57BL/6J mice were imported from Janvier laboratories. The heterozygous mouse line for *Hdac1,2* (*Cx3cr1*$^{creERT/het}$*Hdac1*$^{wt/fl}$*Hdac2*$^{wt/fl}$) was provided by Marco Prinz (Freiburg University), which was further bred in the DZNE mouse facility to generate a homozygous line for *Hdac1,2* (*Cx3cr1*$^{creERT/het}$*Hdac1*$^{fl/fl}$*Hdac2*$^{fl/fl}$). All animal studies complied with the ARRIVE (Reporting of in vivo experiments) guidelines, the German animal welfare law, and were approved by the institutional animal use and care committee in DZNE in agreement with the district government of Upper Bavaria, Germany.

HDAC1/2 depletion in microglia/macrophages

In *Cx3cr1*$^{creERT/het}$*Hdac1*$^{fl/fl}$*Hdac2*$^{fl/fl}$ mice, the activation of Cre recombinase (under the control of Cx3cr1 promoter was induced by tamoxifen (T5648, Sigma-Aldrich). The stock solution of 20mg/ml was prepared in corn oil. 12 and 15 month-old mice were administered 200 μL of tamoxifen solution via intraperitoneal injection thrice, separated by 48 hours. As control animals, tamoxifen injected

(*Cx3cr1*$^{creERT/wt}$*Hdac1*$^{fl/fl}$*Hdac2*$^{fl/fl}$) and (*Cx3cr1*$^{creERT/het}$*Hdac1*$^{wt/wt}$*Hdac2*$^{wt/wt}$) animals were used. A mixed proportion of males and females were used for this study.

METHOD DETAILS

BCG immunization

BCG (RIVM strain -closely related to *M. bovis* BCG Pasteur 1173P2 strain) was reconstituted in 50ml 0.9% NaCl solution on ice. To prevent the degradation of CFU (Colony forming units) due to the sensitivity of BCG-bacteria, BCG suspension was used within 6-7 hours after reconstitution maintaining the efficacy and potency. 12 and 15-months-old C57Bl/6J mice were intravenously (i.v.) injected with 200μl of reconstituted BCG containing 8x10^5-12x10^6 CFU. The control mice received 200μl of 0.9% NaCl solution (i.v.). After one month of immunization, further experiments were executed. Wild-type C57Bl/6J male mice and a mixed proportion of male and female mice for *Cx3cr1*$^{creERT/het}$*Hdac1*$^{fl/fl}$*Hdac2*$^{fl/fl}$ were used for this section of the study.

Stereotactic LPC injections

LPC injections were performed according to an established protocol described in Bosch-Queralt et al.[81] The following coordinates for injections were used: Injection site 1: X = −1/+1, Y =+1.10, Z = −2.30 → −2.25, Injection site 2: X = −1/+1, Y = −0.10, Z = −1.45 → −1.40, Injection site 3: X = −0.55/+0.55, Y = −1.22, Z = −1.45→ −1.40. For volumetric calculations, site 2 was used. Sites 1 and 3 were used additionally when considerable amounts of demyelinated white matter were needed for omics studies. 1μL of LPC was injected at 150nL/minute (1 lesion) and 250nL/minute (multiple lesions). Mice were monitored for 3-4 days post-surgery for any physiological changes.

Immunohistochemistry

To prepare samples for immunohistochemistry, mice were anesthetized with an intraperitoneal injection of 10% ketamine/2% xylazine and perfused intracardially with 4% paraformaldehyde (PFA) with a peristaltic pump (Peri-Star PRO, World Precision Instruments). The brain was removed, postfixed in 4% PFA overnight, and cryoprotected in 30% sucrose in PBS. The tissue was embedded in Tissue-Tek O.C.T, frozen on dry ice, and kept at −80°C until sectioning. For sectioning of the injected brains, a cryostat (CryoStar NX70, Thermo Scientific) was used to cut 16-μm-thick coronal sections, which were directly mounted on Superfrost Plus slides serially. The presence of monastral blue identified the lesions. All sections were kept at −20°C until further processing. For staining, the sections were dried at 37 °C for 30 minutes, rinsed with 1× PBS, and permeabilized for 10 min in 1× PBS containing 0.3% Triton X-100. To prevent non-specific binding, sections were incubated for 1 hour with a blocking solution (2.5% bovine serum albumin, 2.5% fish gelatin, and 2.5% fetal calf serum in 1× PBS). Primary antibodies were diluted in staining solution (25% of blocking solution in 1× PBS) and incubated overnight at 4°C except for Plin2 staining, where the staining solution was supplemented with 0.05% saponin additionally. The next day, sections were further incubated with primary antibodies for 1 hour at RT, washed with 1× PBS, and subsequently incubated with secondary antibodies for 2 hours. After washing with 1× PBS, the sections were incubated with FluoroMyelin (1:400) and DAPI (1:1000) in 1×PBS for 15 minutes. Finally, sections were washed in distilled water and then mounted with mowiol. For stainings with antibodies produced in mice, the Fab fragment-blocking step was performed before adding the blocking solution. All steps were performed at room temperature (RT) unless stated otherwise. For CC1 and perilipin2 staining, heat-induced antigen retrieval was accomplished using (Sodium citrate buffer-10mM Sodium citrate, pH 6.0) before blocking. The primary and secondary antibodies used were the following: IBA1 rabbit (1:1000), IBA1 chicken (1:400), IBA1 guinea pig (1:500), MAC2 rat (1:400), MHCII rat (1:100), PLIN2 rabbit (1:200), Olig2 rabbit (1:250), APC-CC1 mouse (1:100), BCAS1 rabbit (1:500), Alexa Fluor 555 anti-mouse (1:500), Alexa Fluor 555 anti-rabbit (1:500), Alexa Fluor 647 anti-rabbit (1:500), Alexa Fluor 647 anti-Guinea pig (1:500) and Alexa Fluor 647 anti-rat (1:500).

Fluorescence in situ hybridization

The RNAscope Multiplex Fluorescent v2 Assay (Advanced Cell Diagnostics Inc.) was performed according to the manufacturer's instructions for fixed frozen tissue. Brain sections (16-μm-thick) were hybridized with the respective mRNA probes: RNAscope Probe-Mm-Tnf-a, RNAscope Probe-Mm-Il1b-C2, RNAscope Probe-Mm-Abca1, RNAscope Probe-Mm-Abcg1-C2, RNAscope Probe-Mm-Irf7-C2, RNAscope Probe-Mm-Irgm1-C2, RNAscope Probe-Mm-Parp14, RNAscope Probe-Mm-Lamp2-C2 and RNAscope Probe-Mm-Nr1h2 all from Advanced Cell Diagnostics. Additionally, the negative control probe RNAscope 3-Plex Negative Control Probe-Mm and the positive control probe RNAscope 3-plex Positive Control Probe-Mm were used in some sections to assure the specificity and the sensitivity of the signal. The target probes were also combined with immunofluorescence for IBA1 to determine which cells express the genes of interest.

RNA isolation and RT-qPCR

Total RNA was isolated from primary microglia (CD11b$^+$) cells or lesion tissue from adult mouse brains following the manufacturer's instructions of the RNeasy plus mini kit (74134, QIAGEN). The RNA was reverse transcribed with the superscript III first-strand synthesis system (18080051, Invitrogen) using 100ng to 1μg of total RNA. Quantitative PCR was performed using the Power Up SYBR Green Master Mix (A25742, Applied Biosystems) on a Light Cycler 480 Real-time PCR system (Roche). All qPCR reactions were run in triplicate. The primers used for qPCR are mentioned in Table S4.

Confocal microscopy

All images were acquired using confocal microscopy either with a Leica SP5 confocal (20x/0.75 NA air, 63x/1.40NA oil) or the Zeiss LSM 900 (20x/0.8 M27 air, 40x/1.1 W Korr UV-vis- IR water, 63x/1.2 Imm Korr DIC M27-Oil). Additionally, the navigator function of Zeiss was used using (10X/0.30 M27-Air). The different fluorophores were stimulated sequentially using the following laser lines: 405 nm for DAPI, 488 nm for Alexa Fluor 488 (AF488), 561 nm for Alexa Fluor 555 (AF555), and 633 nm for Alexa Fluor 647 (AF647). For reflection^{+} microscopy, the reflected light using the Leica SP5 confocal microscope was used in parallel to imaging the fluorophores as previously described.[82]

Ex-vivo isolation of microglia using magnetic activated cell sorting (MACS) and fluorescence activated cell sorting (FACS)

Mice were anesthetized with an intraperitoneal injection of 10% ketamine/2% xylazine and perfused intracardially with ice-cold 1XPBS with a peristaltic pump (Peri-Star PRO, World Precision Instruments). Primary microglia were isolated from adult mice brains using an Adult Brain dissociation kit (cat-130-107-677, Miltenyi Biotech). Myelin debris and red blood cell removal were performed according to the manufacturer's instructions. Then CD11b^{+} cells were labeled using magnetic beads and isolated using a magnetic column. The cells were further processed and used for different assays. For FACS, we used our previously established isolation protocol using gentleMACS with the Neural Tissue Dissociation Kit (Papain; Miltenyi Biotech) and a final concentration of 45 mM actinomycin D.[83] The dissociated cell suspension was passed through a 70 mm cell strainer (Corning, 52350) before labeling. Subsequently, cells were blocked with mouse FcR-blocking reagent (containing CD16/CD32 Monoclonal Antibody) and then stained for 15 min using Zombie (1:1000) and the antibodies against CD45 (eF450,1:200), CD11b (PerCP-Cy5.5,1:200), Ly6C (BV570, 1:200), Ly6G (PEe610, B, 1:200), F4/80 (PECy7,1:200). Further, the cells were washed with PBS (Sigma, D8537) and viable cells (Zombie negative) were analysed by flow cytometry.

HDAC1 and HDAC2 fluorogenic activity assay

Primary CD11b+ microglia were isolated from young mice treated with saline and aged mice treated with either saline or BCG as described above. Fresh cells were lysed using cell lysis buffer (cell signaling technology Cat# 9803S) followed by ultrasonication (UP200St, Hielscher Ultrasonics) and centrifugation at 14,000g, 4°C for 15 minutes. Following centrifugation, supernatant was collected and used directly for the fluorogenic HDAC1 and HDAC2 assays (BPS Bioscience Cat# 50061, 50062). The HDAC activity assays were performed according to the manufacturer's instructions. Briefly, a master mixture consisting of fluorogenic HDAC substrate 3 (200μM), BSA (1mg/ml) and HDAC assay buffer was prepared and added to a black low binding 96-well microliter plate. The HDAC enzyme (1.4ng/μl HDAC1 or 1ng/μl HDAC2) was added to all wells except for wells designated as blank. Trichostatin A (20μM) served as a control to assess the inhibitory activity and cell lysis buffer without cells was used as the background solution for both blank and positive control. The plate was incubated at 37°C for 30 minutes followed by the addition of undiluted HDAC assay developer and another incubation at room temperature for 15 minutes. Finally, the fluorescence intensity was measured using GloMax®-Multi Detection System at excitation wavelength of 365nm and emission wavelength of 410-460nm. All the measurements were conducted in duplicates and subtracted from the blank before normalizing to the total cell count.

Single-nuclear RNA sequencing (snRNA-seq)

Nuclei isolation and library construction

The mice were perfused intracardially with ice-cold- IX PBS with a peristaltic pump (Peri-Star PRO, World Precision Instruments). The lesioned white matter was dissected from young and aged C57Bl/6J mice on ice using a stereomicroscope (Leica S9E number 10446339). The isolated white matter was flash-frozen in liquid N2 and stored (-80°C) until further processing. The frozen white matter tissues were homogenized in the cold Nuclei EZ Prep lysis buffer (Millipore Sigma) in a 2ml Dounce grinder, followed by clean-up using OptiPrep Density Gradient Medium (Millipore Sigma)[84] The nuclei recovered from the interface of 29% and 35% of the OptiPrep medium were examined and counted using Trypan Blue staining in a hemocytometer. The nucleus suspension of each sample was used for snRNA-seq preparations. Single-nucleus RNA-seq libraries were prepared using Chromium Next Gen Single Cell 3' v3.1 Reagents following the manufacturer's instruction (10X Genomics). The libraries were pooled and sequenced on the NovaSeq 6000 sequencer (Illumina). n = 3 biological replicates per condition were analyzed.

Analysis

Raw sequencing data in fastq format were aligned to *Mus musculus* (mm10) reference genome, quantified, and filtered using 'cell ranger-count (10x genomics, version 6.1.0). Doublet analysis was performed using the 'Doublet Finder' R package (v.2.0.2).[65] The filtered matrix file was further processed using LIGER (Linked inference of Genomic Experimental Relationships)[64] using R version (4.2.2), where replicates from each condition were merged. The datasets were normalized and scaled to account for differences in sequencing, efficiency, and variance between the cells. Integrative non-negative matrix factorization (iNMF) was performed on normalized datasets with the following parameters (K=20, λ=5, threshold 1e-6, max iters-30) followed by joint clustering of cells by quantile normalization and Louvain clustering algorithm in LIGER. Two dimensional representations were generated using uniform manifold approximation and projection (UMAP) as implemented in Liger with the following parameter settings: ('min. dist = 0.3', 'n.neighbors = 30', 'cosine' distance metric). To determine the gene markers for all clusters and for comparing the expression within different datasets, the 'runWilcoxin' function was used with (padj <0.05). As for cell-type identification, a high-quality single-cell RNA-seq of mouse brain dataset served as a reference for our dataset.[85] The expression profiles of differentially expressed genes were

plotted using Violin plot. Re-clustering was performed on existing microglia clusters after sub-setting and re-normalizing using Seurat (version 4.0.6) at resolution 0.25. To determine the significance of cell proportion in each microglia sub cluster between datasets scCODA[78] v.0.1.6 package was used for compositional analysis of the single-cell data. The false discovery rate (FDR) value was set to 0.05 to be able to detect subtle yet biologically relevant changes. In all boxplots, the central line denotes the median, boxes represent the interquartile range (IQR) and whiskers show the distribution except for outliers. For visualizing the QC/alignment metrics of sequencing data, for plotting dot plots and heat maps of differentially expressed genes, scCustomise (v1.1.1) and Seurat (v4.0.6, v4.4.0) were used.

ATAC sequencing

Sample preparation and sequencing

$CD11b^+$ cells were isolated from lesioned brains of mice by MACS as described above and were cryopreserved with 5% DMSO in Mr. frosty container at -80°C (to allow the slow cooling rate to minimize cell lysis) until further processing. Cells (stored at -80°C) were thawed for 2 min at 37°C and then mixed with ice-cold PBS (1:1), followed by centrifugation at 3000 rpm for 5 min at 4°C. Cell pellets were then re-suspended in ice-cold PBS, and cell viability was assessed with Trypan Blue staining. After counting, 20000 viable cells were transferred into a separate tube and centrifuged at 3000 rpm for 7 min at 4°C. ATAC-seq protocol was performed according to the original procedure by[86] with some modifications included for the frozen cells according to.[87] Briefly, cell pellets were re-suspended in ice-cold lysis buffer (10mM Tris-Cl, pH 7.4, 10 mM NaCl, 3mM $MgCl_2$, and 0.1% (v/v) Igepal CA-630) and immediately spun down for 10 min at 500rcf at 4°C. The supernatant was discarded, and cell nuclei were re-suspended in the transposition reaction containing 2μl TDE1 (Nextera Tn5 enzyme), 10μl of 2x TD reaction buffer, and 8μl of H_2O. The reaction was incubated at 37°C for 30 min with gentle shaking (300 rpm). Subsequently, DNA was purified with the ZymoResearch DNA Clear & Concentrator TM-5 and eluted in 10μl of elution buffer (10mM tris-Cl pH 8). DNA was stored at -20°C. The library of transposed DNA fragments was prepared and 10μl of eluted transposed DNA was mixed with 10μl of nuclease-free water, 2.5μl of 25μM PCR primer 1, 2.5μl of 25μM Barcoded PCR Primer 2 (Ad1 and Ad2 PCR primer sequences as in[86] and 25μl of NEBNext High-Fidelity 2x PCR Master Mix (NEB). The reaction was incubated for 5 min at 72°C, 30 sec at 98°C, followed by five cycles of 10 sec at 98°C, 30 sec at 63°C, and 1 min at 72°C. qPCR was then performed to determine the additional number of PCR cycles required for the final library. The profiles of libraries were assessed with the Bioanalyzer2100. The ATACseq libraries were sequenced at 2x76bp paired-end on HiSeq 1500. Each profile was sequenced in two separate lanes. n = 2 replicates per condition were analyzed.

Analysis

FastQC was used to check the quality of raw fastq files. Trimming of Nextera transposase adapters and reads <20 bp with quality cutoff 20 was done using Cutadapt[68]. The trimmed fastq files were aligned to the mm10 genome using bowtie2.[69] The mapped reads were further filtered for mitochondrial reads, reads that are not properly paired and with low mapping quality (phred scale >=30) using BAM tools.[70] Duplicate reads were removed using the Picard tool (Mark Duplicates). Insert sizes were checked with a paired-end histogram to visualize the fragment length distribution (an indicator for the quality of ATAC seq). The aligned BAM files were converted to BED format. Peak calling was performed using MACS2[72] using the settings ('- -nonmodel - - shift-100 - -extsize 200'). The minimum FDR cutoff was set to 0.05, and 'no broad regions ' was set for peak detection. Detection of differential binding sites was done using csaw.[73] Annotation was added to a given set of regions using the 'detailRanges' function in Csaw. This identifies the overlaps between the regions and annotated genomic features such as exons, introns and promoters. We excluded peaks corresponding to unannotated regions and distal regions such as introns (I). Here, the promoter region of each gene was defined as some interval 3 kbp up and 1 kbp downstream of the TSS for that gene. Any exonic features within distance on the left or right side denoted by PE or PI of each supplied region was also considered for analysis. In our case the flanking distance to annotate was (dist =5000). FDR correction was applied on significant p values =<0.05. Visualization of coverage and peaks was performed on Bigwig files using the plot Heatmap of DeepTools[71] and the Integrative Genome Viewer (IGV).[67] The replicates in each condition were merged using the Bigwig merge to generate a combined bigwig file for each condition. Motif analysis was done using the FindMotifsGenome tool[74] of HOMER on the Galaxy platform (https://usegalaxy.eu/).

Bulk-RNA sequencing

Sample preparation and sequencing

RNA was isolated from PFA-fixed OCT-embedded frozen brain sections using the method that digest proteins to free cross-linked RNA.[88] In brief, frozen brain sections (16 μm) were taken out of -80°C and incubated at RT for 5 min, avoiding drying out. 50 μl RNA isolation buffer per sample was prepared and kept on ice, containing 40 μl of PKD buffer (157014133, QIAGEN) with 10 μl proteinase K solution (19131, QIAGEN). The target brain sections (lesioned or unlesioned white matter tissue) were covered with 50 μl isolation buffer and incubated at room temperature for 30 sec. Four lesion tissue sections and five unlesioned tissue were scratched from each slide and condition (aged mice C57Bl/6J treated with saline or BCG) using a stereomicroscope (Olympus SZ51 Model number 1111260100). The brain lysate was collected by pipetting with 200μl tips, snap-frozen in liquid nitrogen, and stored at -80°C until further processing using the method described in Kaya et al.[89] Samples were thawed at RT for 3 min, then vortexed and spun down, followed by the incubation of samples at 56°C for 4 h in a thermal cycler with the lid set at 66°C, checking hourly if the sample was dissolving. After the incubation, vortexing and spinning down the samples, they were transferred into pre-cooled 1.5 ml tubes on ice. Oligo dT25 magnetic beads (61005, Invitrogen) were prepared with three washes of 1x hybridization buffer (HB), which contains 2x SSPE (Life Technologies, Cat#15591-043), 0.05% Tween-20 (1610781, Bio-Rad), 0.05% RNase Inhibitor (2313A, Takara). The

beads were resuspended with half of the original volume in 2x HB for later usage. 10 μl washed dT25 beads (0.1 mg) was added into each sample to reverse cross-linked samples and the samples were further heated at 56°C for one minute. The samples were placed on ice after 10 min incubation at room temperature to allow mRNA hybridization. Then beads were washed two times in 100 μl of ice-cold 1x HB, followed by a subsequent wash using ice cold 1x PBS with 0.1% RNase inhibitor inside. The PBS was removed and resuspended with 15 μl RNase-free water. The sample-beads mixture was incubated at 80°C for two minutes to elute mRNA, then immediately pelleted on a room temperature magnet. The supernatant was rapidly removed containing mRNA and transfer to a new tube and store at -80°C. 1ng mRNA from each sample was taken and continued with the Smart-seq2 protocol as described in Safaiyan et al.[19] and Kaya et al.[89]. Libraries were sequenced 2x150 reads base pairs (bp) paired-end on Illumina X-ten platform (BGI) to a depth of $8x10^6$-$30x10^6$ reads/sample. n=6 biological replicates per condition were analyzed for lesion tissue and n=5 biological replicates per condition was analyzed for unlesioned tissue.

Analysis

FastQC was used to check the quality of fastq files. Low-quality reads and adapters were trimmed using Trim galore and Cutadapt using the following parameters (reads <20 bp with quality cutoff 20). The trimmed FASTQ files were mapped to the mm10 reference genome using STAR.[75] The mapped reads (of lesioned or unlesioned tissue sections) belonging to the same slide were merged using the merge BAM files tool in Galaxy version 4. To quantify the number of reads mapping to the exons of each gene, feature counts[76] was used. Further, to compare the expression of single genes between different conditions, differential analysis was performed using Deseq2.[77] The minimum FDR cutoff was set to 0.05 for further analysis. Additionally, for visualization of gene expression over samples between conditions, a heatmap was plotted of the computed z-scores using Galaxy version 4.11 (https://usegalaxy.eu/).

Chromatin immunoprecipitation sequencing (ChIP-seq)

Sample preparation and sequencing

$CD11b^+$ cells were isolated from the brains of aged mice treated with saline or BCG by MACS, as described above. The isolated cells were fixed with formaldehyde solution at a final concentration of ~1 % for 10 min, followed by quenching using Glycine at a concentration of 1.25M for 5 minutes at RT to stop fixation. The cross-linked cells were gently washed with ice-cold HBSS containing protease inhibitor cocktail -25X and were stored at (-80° C) until further processing. Diagenode ChIP-seq/ChIP-qPCR Profiling service (Diagenode Cat# G02010000) prepared the chromatin using the iDeal ChIP-seq kit for Histones (Diagenode Cat# C01010059). The cell nuclei were lysed, and chromatin was sheared using a Bioruptor® Pico sonication device (Diagenode Cat# B01060001) combined with the Bioruptor® Water cooler for 8 cycles using a 30'' [ON] 30'' [OFF] settings. Shearing was performed in 0.2ml Bioruptor® Pico Microtubes with the following cell number: 1 million in 100μl. An aliquot of this chromatin was used to assess the size of the DNA fragments obtained by High Sensitivity NGS Fragment Analysis Kit (DNF-474) on a Fragment Analyzer™ (Agilent). ChIP was performed manually following the protocol of the kit as mentioned above. Chromatin corresponding to 94ng was immunoprecipitated using the following antibodies and amounts: H3K4me3 (Diagenode C15410003, Lot A8034D) and H3K27ac (C15410196, Lot A1723-0041D). Chromatin corresponding to 1% was set apart as input. qPCR analyses were made to check ChIP efficiency using KAPA SYBR® FAST (Sigma-Aldrich) on LightCycler® 96 System (Roche). IPs with a negative control isotype (IgG) were also performed in parallel. Libraries were prepared using IP-Star® Compact Automated System (Diagenode Cat# B03000002) from input and ChIP DNA using MicroPlex Library Preparation Kit v3 /96 rxns (Diagenode Cat# C05010002) with 24 UDI for MicroPlex v3 - Set I (Diagenode Cat# C05010008). Optimal library amplification was assessed by qPCR using KAPA SYBR® FAST (Sigma-Aldrich) on Light Cycler® 96 System (Roche) and by using High Sensitivity NGS Fragment Analysis Kit (DNF-474) on a Fragment Analyzer™ (Agilent). Libraries were then purified using Agencourt® AMPure® XP (Beckman Coulter) and quantified using Qubit™ dsDNA HS Assay Kit (Thermo Fisher Scientific, Q32854). Finally, their fragment size was analyzed by High Sensitivity NGS Fragment Analysis Kit (DNF-474) on a Fragment Analyzer™ (Agilent). Libraries were pooled and sequenced with paired-end reads of 50bp length on an Illumina Novaseq 6000 to a depth of 100 million reads/sample. n=2 independent replicates per condition were used for each histone mark. Each replicate was a pool of 3 animals.

Analysis

Quality control of sequencing reads was performed using FastQC. The raw reads with a phred score > 30 were further used to align to the mm10 genome using bowtie2.[69] Duplicate reads were removed using the Picard tool (Mark Duplicates). Quality control of Chip-seq preparation was done by determining the correlation between samples (a method to know if Chip-seq samples are more enriched than input samples using multiBamSummary) and QC modules of Deep tools plot correlation. To detect the enriched regions marked by H3K4me3 and H3K27ac marks, peak calling was performed using MACS2[72] normalized to the input (control) using the parameters –(create_model - - mfold (5-50) - -bw 300'). The minimum FDR cutoff was set to 0.05, and peaks were called using the default (narrow) setting.[90] The average fraction of reads in peaks for H3K4me3 was 28.3% in the BCG treated group and 27.15% in the control group. For H3K27ac, the average fractions were 7.7% in the BCG treated group and 6.1% in the control group. Detection of differential binding sites was done using csaw.[73] FDR correction was applied on significant p values =<0.05 with $\log_2$FC >1. The number of differential features identified were 178 for H3K4me3 and 8048 (P, PE) for H3K27ac, respectively. To find the genes enriched for H3K4me3 and H3K27ac marks out of genes common for (snRNA and ATAC), the bed file of 833 genes was prepared from the UCSC table browser, and differential binding was performed using Csaw. Visualization of coverage and peaks was performed on Bigwig files using the plot Heatmap of DeepTools[71] and the Integrative Genome Viewer (IGV).[67] The replicates in each condition were merged using the Bigwig merge to generate a combined bigwig file for each condition. Motif analysis for H3K4me3 and H3K27ac

was done using the FindMotifsGenome tool Heinz et al.[74] of HOMER on the Galaxy platform (https://usegalaxy.eu/) in which GC normalization was based on the sequences randomly selected from the genome matched for GC% content.

Chromatin immunoprecipitation qPCR (ChIP-qPCR)

CD11b$^+$ cells were isolated from the brains of aged mice, young mice, and genetically modified *Cx3cr1*$^{creERT/wt}$*Hdac1*$^{fl/fl}$*Hdac2*$^{fl/fl}$ and *Cx3cr1*$^{creERT/het}$*Hdac1*$^{fl/fl}$*Hdac2*$^{fl/fl}$ mice by Magnetic activated cell sorting (MACS). Chromatin immunoprecipitation was performed on the isolated cells as described above. 400ng Chromatin was immunoprecipitated using the following antibody and amount: anti-H3K27ac DGN (Cat# C15410196) 1 μg. Chromatin corresponding to 1% was set apart as Input. Real-time quantitative PCR (RT-qPCR) analyses were conducted using KAPA SYBR® FAST (Sigma-Aldrich) on a LightCycler® 96 System (Roche). Results were expressed as percentage recovery, calculated using the formula: % recovery = 2^(Ct_input-dilution factor)-Ct_sample)*100. The specificity of the immunoprecipitated DNA was verified by qPCR. To assess the ChIP efficiency, negative control isotype (IgG) and specific primer pairs targeting a positive control region (*Actb*) and a negative control region (*MyoEx2*) for H3K27ac were employed. The primer sequences used for ChIP-qPCR were designed surrounding the potential H3K27ac binding region obtained from ChIP- seq data and are listed in Table S4.

GO enrichment analysis

Gene ontology (GO) enrichment analysis was done using (http://www.geneontology.org/) database[91] using the annotation dataset – GO biological process complete and a reference list of *Mus musculus* species. Background correction for all GO analysis was performed as described in Timmons et al.[92] Fisher's exact test with FDR correction was applied to report statistically significant enriched terms. Revigo[79] and Cytoscape (version 3.9.1) were used for enrichment maps of GO-enriched terms.

Image analysis

To quantify the demyelination volume and the IBA1$^+$ volume, the area of demyelination shown by negative FluoroMyelin staining and the area of clustered IBA1$^+$ cells, respectively, was measured in consecutive sections of a lesion, which were separated by a known distance. The lesion volume was then calculated according to the truncated cone volume formula in an automated fashion using IPython 2.7. as described in Bosch-Queralt et al.[81] For the quantification of myelin-loaded IBA1$^+$ cells, crystal-loaded IBA1$^+$ cells, MAC2$^+$IBA1$^+$ cells, MHCII$^+$IBA1$^+$ cells, CC1$^+$ cells, and foam cells, the cells were counted manually in high magnification images of the lesion using the Cell Counter plug-in in Fiji.[80] The pictures were coded so that the analysis would be blinded. The quantifications of lipid-loaded microglia, MHCII$^+$ microglia, MAC2$^+$ microglia *Tnf*$^+$*Il1ß* $^+$ mRNA in microglia were performed by counting manually in the images acquired. For quantifying the *Abca1*, *Abcg1, Irf7, Irgm1, Parp14, lamp2* and *Nr1h2* mRNA particles in the fluorescence in situ hybridization, the positive particles were quantified in the mask created by the IBA1$^+$ signal in an automated fashion using Fiji.

Statistics and reproducibility

Data values are represented as mean ± SD. Statistical analysis was performed with Graph Pad Prism (Graph Pad Software). The number of animals used for the experiments is indicated as a single bubble in all graphs or shown in the methodology. Normality tests (for e.g. Shapiro -Wilk test) were used to confirm the normal distribution of our data. Thus, a two-tailed student's t-test, Welch's t-test or Mann Whitney test was applied to compare the two groups and one and two way *ANOVA* with Tukey's post hoc test or Bonferroni correction was used to compare more than two groups. For measuring statistical differences in RT-qPCR results, the -2$^{\Delta\Delta Ct}$ value was employed, and the -2$^{\Delta\Delta Ct}$ values were subjected to the test. A *P* value of $\leq$0.05 was considered significant in all cases. For histological analyses depicted in Figures 4D, 4E, 4J, 4M, 4N, 6C, 6E, 6J, 6L, 6M, 6O, S5A, S5D, S6F, and S7A–S7L three to five brain sections were quantified per mouse to account for variability within the biological sample. For all experiments, 12 and 15 months old mice and 3 months old young mice were taken except snRNA and ATAC seq, where 15 and 20 months old mice were used.